

Coupled hydro-mechanical analysis of two unstable unsaturated slopes subject to rainfall infiltration

Kuo-Hsin Yang^{a,*}, Ryosuke Uzuoka^b, Joseph Ng'ang'a Thuo^a, Guan-Liang Lin^a, Yuta Nakai^b

^a Department of Civil and Construction Engineering, National Taiwan University of Science and Technology (Taiwan Tech), 43, Sec. 4, Keelung Rd., Taipei 106, Taiwan

^b Department of Civil and Environmental Engineering, Tokushima University, Minamijosanjima-cho 2-1, Tokushima, Japan

ARTICLE INFO

Article history:

Received 19 April 2016

Received in revised form 5 November 2016

Accepted 9 November 2016

Available online 11 November 2016

Keywords:

Coupled hydro-mechanical analysis

Unsaturated soil

Finite element

Slope instability

ABSTRACT

This paper presents a case study and numerical investigation of two unstable unsaturated slopes along the Taipei Maokong Gondola system. One slope collapsed because of torrential rainfall during Typhoon Jangmi in September 2008, and another nearby slope developed excessive deformation under consecutive wetting and drying cycles. Recorded rainfall, measured soil parameters, site geology, and slope geometry were used in coupled hydro-mechanical finite element analyses to investigate the failure and deformation mechanisms of these two slopes. The stress paths of these two slopes were also examined and are discussed in this paper. The numerical results demonstrated that the coupled hydro-mechanical analysis satisfactorily predicted the failure and deformation characteristics of the two unstable slopes. In the collapse case, failure occurred at a shallow depth when the surficial residual soil was saturated. The slope failure was attributed to a decrease in soil shear strength when the matric suction gradually decreased as rainfall progressed. In the excessive deformation case, the numerical results suggested that pore water pressure (PWP) varied at shallow depths under wetting and drying cycles, whereas positive PWP accumulated at the soil–rock interface and induced non-uniform lateral flows parallel to the interface. The accumulated positive PWP at the interface mobilized a considerable plastic deformation in the soil. Examination of the relationships between the slope factor of safety and the corresponding hydrological data (i.e., rainfall and soil PWP) revealed a positive correlation between the slope factor of safety and accumulated rainfall. The factor of safety predicted by the infinite slope equation significantly varied with the input of PWP. This study demonstrated that the infinite slope equation using the PWP measurements obtained from the lower half of the slope could effectively predict the slope factor of safety.

© 2016 Elsevier B.V. All rights reserved.

1. Introduction

Typhoons and heavy rainfall from extreme weather events often cause natural disasters such as floods, landslides, and debris flows. Rainfall-induced slope failures are major geotechnical disasters and have been frequently reported in many regions worldwide. The limit equilibrium method is the most widely used technique for slope stability analyses and engineered slope designs. In conventional practice, the effects of rainfall on a slope were modeled by raising the groundwater table (GWT) level in slope stability analyses. However, this approach only considers the saturated slope failures below the GWT, and may overlook the influence of rainfall infiltration on unsaturated soil conditions, resulting in a possible misinterpretation of the failure mechanism and an inaccurate prediction of the corresponding factor of safety (FS).

Analytical, statistical, probabilistic, and numerical methods have been employed to assess the hydrological response and associated stability of unsaturated slopes subject to transient infiltration flow (Cho, 2014, 2016; Da Costa and Sagaseta, 2010; Davies et al., 2014; Gui and Wu, 2014; Lu et al., 2013; Urciuoli et al., 2016; Wu et al., 2015a, 2015b). Studies have indicated that for shallow residual slopes, the potential failure surface could be entirely above the phreatic level which may not have significant variation with rainfall infiltration (Cho and Lee, 2002; Collins and Znidarcic, 2004; Gerscovich et al., 2006; Kim et al., 2004). The failure mechanisms of this residual layer, when wetted, primarily involve rainfall-induced wetting front advancement, which causes suction losses, leading to a decrease in soil shear strength (Cho and Lee, 2002; Iryo and Rowe, 2005; Kim and Borden, 2013; Muntohar and Liao, 2010; Qi and Vanapalli, 2015; Thuo et al., 2015; Yoo and Jung, 2006). Studies have discovered that when unsaturated soil slopes are subject to consecutive wetting and drying cycles, the soil moisture and PWP exhibit spatiotemporal variations within the slopes. Slope stability is directly influenced by rainfall-induced PWP, which is a function of infiltration rate, soil hydraulic characteristics, and slope geometry (Alonso et al., 1995; Chen et al., 2015; Collins and

* Corresponding author.

E-mail addresses: khy@mail.ntust.edu.tw (K.-H. Yang), uzuoka@tokushima-u.ac.jp (R. Uzuoka), d10305813@mail.ntust.edu.tw (J.N. Thuo), andy540882003@gmail.com (G.-L. Lin), nakaitoku@gmail.com (Y. Nakai).

Znidarcic, 2004; Eichenberger et al., 2011; Hossain et al., 2013). Therefore, assessing the hydrological response of unsaturated slopes subject to rainfall infiltration is critical and challenging, especially when determining the variation of PWP within slopes (Baeza and Corominas, 2001; Godt et al., 2009; Lee and Park, 2015; Mori et al., 2011; Morse et al., 2014; Thuo et al., 2015).

Coupled and uncoupled hydro-mechanical analyses based on the framework of unsaturated soil mechanics have recently been performed to describe the physical responses of unsaturated soil under infiltration conditions (i.e., variation of soil moisture, matric suction, effective stress, soil shear strength, and slope stability) (Casini, 2013; Nogueira et al., 2011; Oh and Lu, 2015; Qi and Vanapalli, 2015; Wu et al., 2015a, 2015b). In the uncoupled analysis, a seepage analysis is first utilized to predict pore water pressures within the analyzed slope in a given time increment, and the generated pore water pressures are then used as input in deformation or stability analyses (Qi and Vanapalli, 2015; Cai and Ugai, 2004; Yoo and Jung, 2006). The accuracy and computational efficiency of the uncoupled analysis highly depends on the selected time increments. The accuracy of the uncoupled analysis is ensured by using a small time increment. However, a too-small time increment may entail unnecessarily long computing times (Huang and Lo, 2013; VandenBerge et al., 2015). In addition, the change of pore water pressure caused by the soil deformation (i.e., change of soil volume) is not taken into account in the uncoupled analysis. In contrast, the coupled analysis robustly integrates the above two computation procedures together; the soil hydraulic and mechanical responses are calculated simultaneously in the coupled analysis. Compared with the uncoupled analysis, Qi and Vanapalli (2015) found the coupled analysis produced a reasonably well defined wetting front and a lower critical FS for unsaturated soil slopes. Oh and Lu (2015) commented that the coupled analysis could lead to more accurate assessment of slope stability under infiltration conditions and demonstrate a better physical representation of water flow and stress variation within unsaturated soils.

Although numerous hydro-mechanical analyses were performed, focus was placed on predicting hydrological responses and slope factor of safety. Limited studies have reported the deformation and stress paths of slopes subject to wetting and drying cycles. In current practice, slope deformation of unstable slopes is often monitored using inclinometers. However, the stress state and stability levels are difficult to interpret from monitored slope deformation information. The desirable information on stress and stability could be readily obtained using coupled hydro-mechanical analyses, where the deformation of unsaturated soil is included and calibrated according to the monitored slope deformation.

This paper presents a case study and numerical investigation of two unstable unsaturated slopes along the Taipei Maokong Gondola system. One slope (Slope 1) collapsed because of torrential rainfall during Typhoon Jangmi on September 2008, and another nearby slope (Slope 2) developed excessive deformation under consecutive wetting and drying cycles. A series of coupled hydro-mechanical finite element analyses were performed based on the framework of unsaturated soil mechanics. Field and laboratory test data obtained from site investigations were applied as input material properties and initial conditions in the numerical model. The objectives of this paper are as follows: (1) to investigate the failure and deformation mechanisms of these two unstable slopes; (2) to evaluate the developed stress state and stability levels according to the monitored slope deformation information; (3) to examine the relationships between hydrological data (i.e., rainfall and soil PWP) and the corresponding slope FS. This study demonstrated the suitability and applicability of hydro-mechanical analysis to predict the failure and deformation of unsaturated slopes by using the selected case studies. The causes of slope failure and deformation are discussed and remediation measures based on the revealed failure and deformation mechanism are suggested for mitigating potential landslide disasters.

2. Formulations of coupled hydro-mechanical analysis

2.1. Governing equation

To consider both the deformation and seepage flow within partially saturated soil, the fully coupled flow deformation module was implemented into the PLAXIS (version 2D 2015) finite element (FE) program. Galavi (2010) reported detailed finite element formulations and verification for coupled hydro-mechanical analysis. The coupled hydro-mechanical formulation was developed based on Biot's three dimensional consolidation theory (Biot, 1941), which involves two sets of governing equations, the partial differential force equilibrium and water continuity equations, namely, that form the coupling matrix (Eq. (1)) in which the displacement and PWP can be solved simultaneously.

$$\begin{bmatrix} \underline{K} & \underline{Q} \\ 0 & -\underline{H} \end{bmatrix} \begin{bmatrix} \underline{u} \\ \underline{p} \end{bmatrix} + \begin{bmatrix} 0 & 0 \\ \underline{C} & -\underline{S} \end{bmatrix} \begin{bmatrix} \frac{d\underline{u}}{dt} \\ \frac{d\underline{p}}{dt} \end{bmatrix} = \begin{bmatrix} \underline{f}_u \\ \underline{G} + \underline{q}_p \end{bmatrix} \quad (1)$$

where \underline{K} , \underline{H} and \underline{S} are the stiffness, permeability, and compressibility matrix, dependent on the state of stress and suction; \underline{Q} and \underline{C} are the coupling matrices; \underline{u} and \underline{p} are vectors corresponding to incremental deformation and pore pressure, respectively; \underline{f}_u , \underline{q}_p and \underline{G} are vectors of external load increment, input flux on boundaries, and the vertical flow driven by gravity, respectively. Given that the third phase (pore air) within the surficial layer of the slope is essentially connected to the atmosphere, the air pressure u_a in the unsaturated soil elements is assumed to be a constant value, resulting in the increment of $u_a = 0$. This assumption enables the removal of the effect of u_a from the analysis. This approach has been adopted by many researcher in their studies of unsaturated slopes subject rainfall and seepage (Oh and Lu, 2015; Qi and Vanapalli, 2015; Zhang et al., 2014). Three-phase (soil, water and air) coupled analysis should be considered when unsaturated earth structures are subject to seismic loadings, in which the unsaturated soils also could be liquefied during earthquakes (Matsumaru and Uzuoka, 2016).

2.2. Transient seepage analysis and soil–water characteristics

Before performing the coupled hydro-mechanical analysis, a transient seepage analysis was conducted to generate an initial PWP distribution. Soil deformation was not considered during the modeling of initial hydrological conditions. The applied governing equation for transient flow within an unsaturated medium was derived from Richards (1931).

$$k_x \frac{\partial^2 h}{\partial x^2} + k_y \frac{\partial^2 h}{\partial y^2} = \frac{\partial \theta}{\partial t} = m_w \rho_w g \frac{\partial h}{\partial t} \quad (2)$$

where k_x and k_y represent the hydraulic conductivities in the x- and y-direction (k value is a function of matric suction); h is the total hydraulic head of flow; θ is the volumetric water content; m_w is the coefficient of water volume change (slope of the water characteristic curve); ρ_w is the density of water; g is the acceleration of gravity and t is the time.

In this study, van Genuchten-Mualem's model (Mualem, 1976; van Genuchten, 1980) was applied to define the relationship between matric suction and soil volumetric water content and to estimate changes in hydraulic conductivity with matric suction. The soil–water characteristics and k-function curves are expressed as:

$$\theta = \frac{\theta - \theta_r}{\theta_s - \theta_r} = \left[\frac{1}{1 + \{\alpha(u_a - u_w)\}^n} \right]^{1-1/n} \quad (3)$$

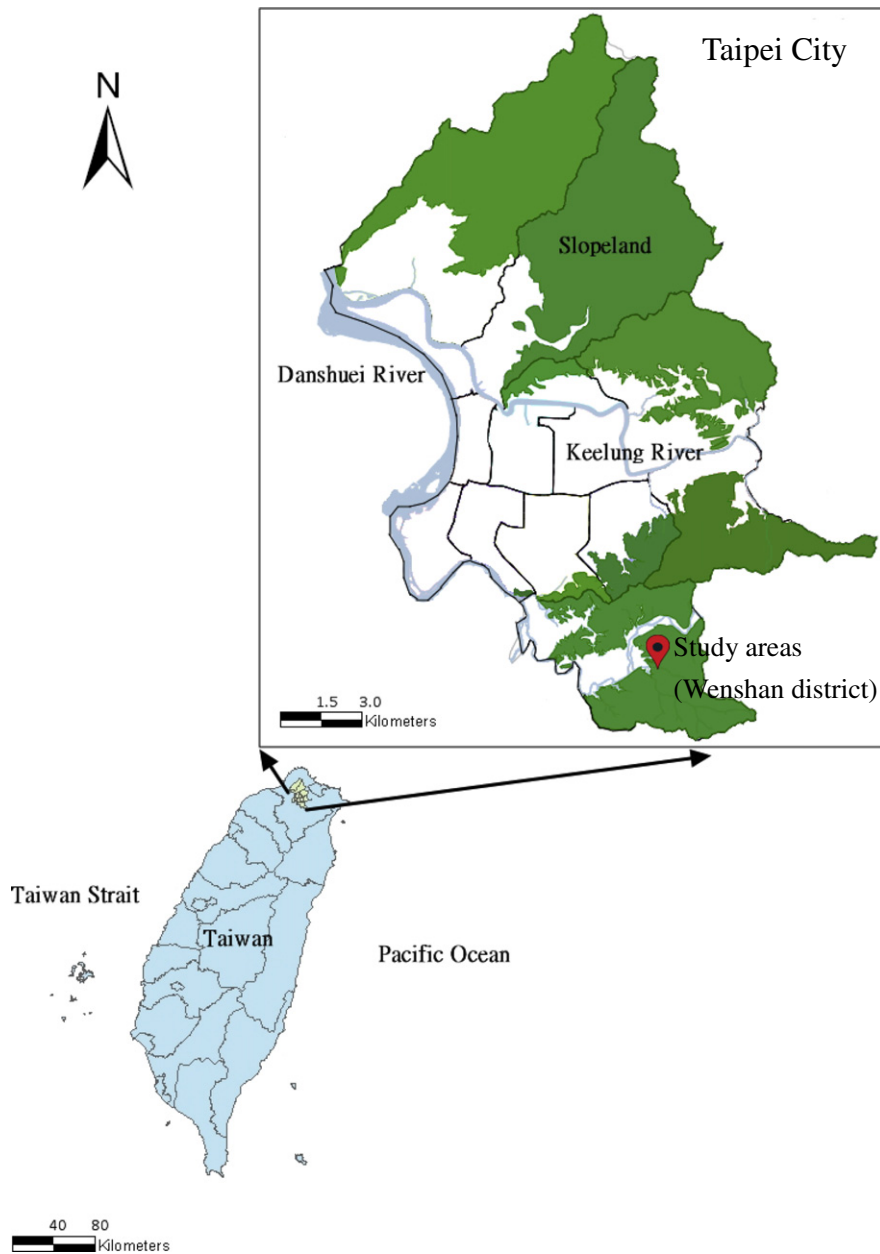


Fig. 1. Map of slope case study location in Taipei City. The solid line inside the map of Taipei City indicate the boundaries of 12 administrative districts.

$$k_{rel} = \frac{k}{k_s} = \theta^{1/2} \left[1 - \left(1 - \theta^{1/(1-1/n)} \right)^{1-1/n} \right]^2 \quad (4)$$

where θ is the normalized volumetric water content; θ_s is the saturated volumetric water content; θ_r is the residual volumetric water content; $(u_a - u_w)$ is the matric suction (where u_a and u_w are the pore air and pore water pressures, respectively); α and n are the curve fitting parameters in van Genuchten-Mualem's model; k_{rel} is the relative hydraulic conductivity; k is the hydraulic conductivity at any soil degree of saturation; k_s is the saturated hydraulic conductivity.

2.3. Effective stress and shear strength under unsaturated conditions

Two numerical approaches have been used to model unsaturated soil behavior; one group of researchers applied soil models based on two stress-state variables (Alonso et al., 2003; Cho and Lee, 2001; Qi and Vanapalli, 2015; Zhang et al., 2005), whereas another group

employed the soil models according to the effective stress principle (Borja et al., 2012; Chen et al., 2009; Ehlers et al., 2004; Matsumaru and Uzuoka, 2016; Oh and Lu, 2015; Rojas et al., 2015; Wu et al., 2015a, 2015b). The latter numerical approach based on the generalized effective stress principle was adopted in this study. The suitability and applicability of the generalized effective stress principle to predict the unsaturated soil behavior (i.e., shear strength, deformation, and pore pressure generation) has been widely validated by many researchers (Borja et al., 2012; Chen et al., 2009; Ehlers et al., 2004; Matsumaru and Uzuoka, 2016; Oh and Lu, 2015; Rojas et al., 2015; Wu et al., 2015a, 2015b). Sheng et al. (2008) concluded that despite challenges associated with obtaining effective stress parameters of soil, the use of Bishop's effective stress for unsaturated soil could lead to smooth transitions between saturated and unsaturated states and simplify constitutive relations and shear strength failure criteria. While the adopted framework presents practical advantages, such approach also has some limitations, especially in the present of complex processes such as collapsible soils and hydraulic hysteresis under drying and wetting cycles.

An effective stress under unsaturated conditions, originally proposed by Bishop (1954), was defined as:

$$\sigma' = (\sigma - u_a) + [S_e(u_a - u_w)] \quad (5)$$

where σ' and σ are the effective and total stress, respectively; $(\sigma - u_a)$ is the net normal stress; $(u_a - u_w)$ is the matric suction; S_e is the effective saturation, expressed as:

$$S_e = \frac{S - S_r}{S_s - S_r} \quad (6)$$

where S is the degree of saturation; S_s is the degree of saturation at fully saturated state ($= 100\%$); S_r is the degree of saturation at residual state. Note that the effective stress defined in PLAXIS (Eq. (5)) is identical to Eq. (7) based on the suction stress concept proposed by Lu and Likos (2004, 2006) because $\Theta = S_e$.

$$\sigma' = (\sigma - u_a) - \sigma^s = (\sigma - u_a) + [\Theta(u_a - u_w)] \quad (7)$$

From Eq. (7), the suction stress σ^s can be expressed as a suction stress characteristic curve (SSCC), which is a function of matric suction (Lu and Likos, 2006; Lu et al., 2010).

$$\begin{aligned} \sigma^s &= -\Theta(u_a - u_w) = -\frac{\theta - \theta_r}{\theta_s - \theta_r} (u_a - u_w) \\ &= -\psi \left[\frac{1}{1 + [\alpha(u_a - u_w)]^n} \right]^{1-1/n} \end{aligned} \quad (8)$$

where parameters α and n are the curve fitting parameters in van Genuchten-Mualem's model. Suction stress can be perceived as an equivalent isotropic confining stress or mean intergranular stress acting on soil particles. When soil is saturated (i.e., $\Theta = S_e = 1$), the σ^s changes to a positive PWP and the suction-based effective stress then coincides with Terzaghi's effective stress. The suction stress concept has been validated experimentally by Kim et al. (2016), Oh and Lu (2015), and Morse et al. (2011).

Soil shear strength was calculated using the Mohr–Coulomb failure criterion.

$$\tau = c' + \sigma' \tan \phi' \quad (9)$$

where τ is the soil shear strength; c' and ϕ' are the effective cohesion and friction angle; σ' is the effective normal stress on the failure plane. When soil is partially saturated, substitute σ' in Eq. (7) into Eq. (9):

$$\tau = c' + (\sigma - u_a) \tan \phi' + \Theta(u_a - u_w) \tan \phi' \quad (10)$$

This equation (Eq. (10)) is known as the extended Mohr–Coulomb failure criterion proposed by Vanapalli et al. (1996), which can describe and predict the nonlinear relationship between soil strength and suction (Qi and Vanapalli, 2015; Zhang et al., 2014). When soil is saturated, Eq. (10) reverts to the form in Eq. (9), which is valid for saturated conditions, and incorporates the effective stress principle.

3. Case histories and site conditions

Two unstable slopes along the Taipei Maokong Gondola system situated in the southern mountain area of Taipei City were studied (Fig. 1). Taipei City, the capital and the largest metropolitan city of Taiwan, covers 271.8 km² and has a total population of approximately 2,623,000 people (population density of approximately 9760 people/km²). Taipei City is located at the central and slightly eastern section of the Taipei Basin. Approximately 55% of the area of Taipei city is covered by slopeland (green-colored area, Fig. 1). The geological composition in the northern region primarily consists of igneous rock layers

formed by the Tatun Volcano group and the remaining area of Taipei City mostly consists of sedimentary rock and alluvium deposits.

Taipei is at relatively high risk of natural disasters caused by heavy rainfall because it is situated in the western Pacific typhoon region. On average, 3.4 typhoons attack Taiwan annually. Taipei City has an annual average precipitation of 2663 mm/year in flatland and 4474 mm/year in slopeland, which is mostly concentrated during the typhoon and heavy rainfall seasons, and occurs from May to October. Because Taiwan is also located on the convergent boundary between the Eurasian Plate and the Philippine Sea Plate, relative movement of these plates causes rock fragmentation and complex fractures in Taiwan's geological environment. Currently, 6.8% of Taipei City area is classified as geologically sensitive because of special geological environments and potential geological hazards. Thus, typhoons and heavy rains frequently result in many slope failures, landslides, and debris flows.

In the presented case studies, Slope 1 (near the No. 16 support tower of the Gondola system) collapsed because of torrential rainfall during Typhoon Jangmi during September 26–28, 2008 (Fig. 2a). The collapsed area was 20–40 m wide and 220 m long at an elevation of 150–280 m above sea level. The estimated total volume of collapsed soil mass is approximately 23,700 m³. The meteorological record indicated that the total precipitation in that region during the typhoon reached 500 mm in 3 days. The Maokong Gondola ride was suspended for sixteen months because of concerns that the foundation of its Gondola pylons could be damaged. Thereafter, massive geotechnical investigation, instrumentation, and remediation programs (Fig. 2) were implemented to ensure

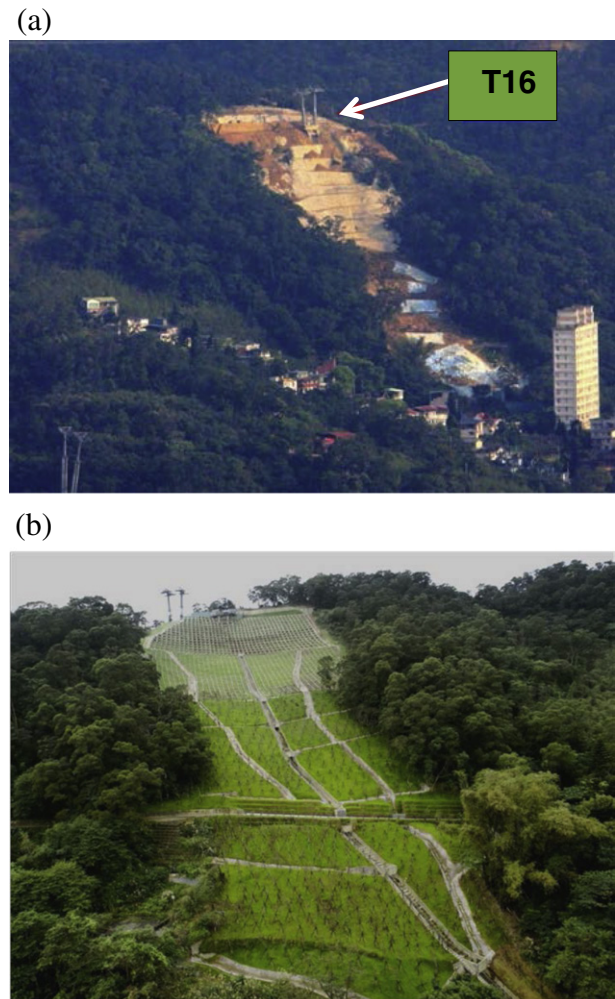


Fig. 2. Slope 1 near No. 16 support tower: (a) slope failure; (b) retrofitted using grid-type slope protection and surface drainage/discharge system.

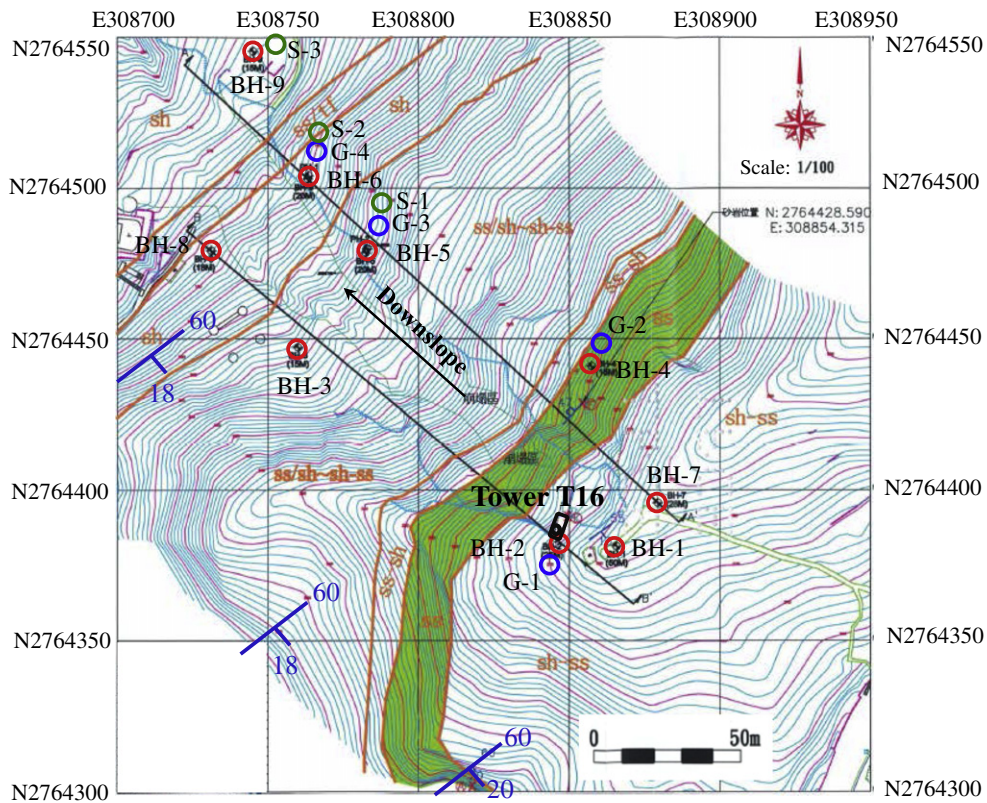


Fig. 3. Locations of boreholes (BH), permeability tests (G) and suction measurement (S) in Slope 1.

the stability of the adjacent slopes and the safety of the gondola system. During monitoring, the inclinometer reading revealed that Slope 2, which was 1.8 km away from Slope 1, developed excessive deformation (>30 mm) under consecutive wetting and drying cycles over a period of 5 years.

Subsurface soil and ground water information along the inspected slopes was obtained from in-situ and laboratory tests in the site investigation program conducted by the Taiwan Professional Geotechnical Engineers Association. Fig. 3 displays the locations of boreholes, permeability tests, and the suction measurement of Slope 1. Detailed results of material properties obtained from laboratory tests are summarized in Table 1 and further discussed later. Fig. 4 depicts the cross-section of the slope geometry and geological settings of the two slopes. The average slope angles of Slopes 1 and 2 are $\beta = 26^\circ$ and 29° , respectively, which is close to the effective friction angles (i.e., the angle of repose) of the residual soil.

The upper layer of the slopes is characteristically composed of residual soil with a depth from 2 to 6 m. The residual soil consist of silty sand (SP), low-plastic silt, (ML) and limited low-plastic clay (CL with plasticity index $PI = 10\text{--}15$) decomposed from the underlain weathered

sandstone and shale. The residual soil is susceptible to moisture variation, often leading to strength and stiffness reduction when wetted. The SPT values of the residual soils in two slope cases range from $N_{60} = 12$ to 35 with mean of 21 and standard deviation of 8. The mean SPT value $N_{60} = 21$ was used to represent the average soil condition in Slope 1, while higher SPT value $N_{60} = 28$ was selected for Slope 2 because the soil near the inclinometer, located at the slope crest, is stiffer than the soil below the crest. The selected SPT-N values fall within ± 1 standard deviation of the mean.

The Miocene Taliao formation and Shihti formation forms the slope bedrock, which consists of sandstone (SS), shale, (SH) and a sandstone-shale interbedded layer (SS-SH). This type of geological composition is typical for eastern and southern mountain slopes in Taipei City. The attitude (strike/dip angle) of rock layers of the two investigated slopes was $N50^\circ\text{--}60^\circ/10^\circ\text{--}20^\circ\text{SE}$ (Fig. 3). Based on the attitude of the rock layers, the two slopes were classified as anaclinal slopes (Fig. 4). The GWT monitored from boreholes varied from 8 to 12 m below the slope surface and the residual soil layer was entirely above the GWT under normal conditions.

Table 1
Material properties.

Soil layer	Soil model	Analysis type	γ_{unsat} (kN/m ³)	γ_{sat} (kN/m ³)	Poisson ratio, ν' , ν_u	Cohesion, c' , $q_u/2$ (kPa)	Friction angle, ϕ' ($^\circ$)	Saturated hydraulic conductivity, (cm/s)	Modulus E, E_u (kPa)
Residual layer (F)	Hardening soil	Unsaturated drained	19.5	20.1	0.3	6 ^a , and 10 ^b	27 ^a , and 30 ^b	$k_{s,v} = 2.76 \times 10^{-4}$ $k_{s,h} = 4.14 \times 10^{-4}$	5651 ^a , 7800 ^b
Sandstone (SS)	Mohr-Coulomb	Saturated undrained	24.6	25.4	0.495	679	0	1×10^{-6}	1.78×10^6
Shale (SH)	Mohr-Coulomb	Saturated undrained	23.6	24.5	0.495	256	0	5×10^{-13}	4.91×10^5
Sandstone and shale interbedded (SH-SS)	Mohr-Coulomb	Saturated undrained	24.2	24.9	0.495	467	0	2×10^{-10}	1.14×10^6
Shale interbedded with few sandstone (SH/ss)	Mohr-Coulomb	Saturated undrained	23.8	24.9	0.495	306	0	1×10^{-11}	876×10^5

^a Soil shear strength properties for Slope 1.

^b Soil shear strength properties for Slope 2.

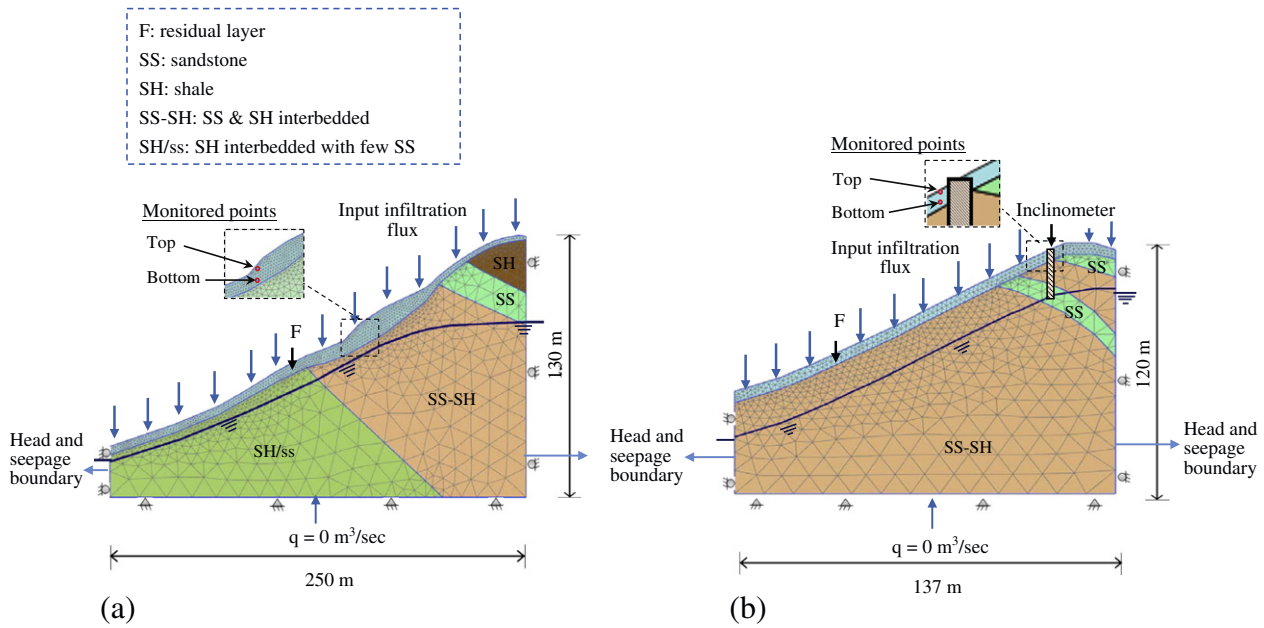


Fig. 4. Geologic profiles and numerical models: (a) Slope 1; (b) Slope 2.

4. Numerical simulation

4.1. Numerical model and boundary conditions

Fig. 4 displays the two-dimensional FE models used for Slopes 1 and 2. The slope geometry was constructed according to topographic maps and the subsurface soil profiles were interpolated from the borehole logging readings displayed in Fig. 3. Slopes 1 and 2 consist of a total of 2791 and 3195 fifteen-node triangular elements, respectively. Fine-element meshes were specified for the residual soil layers whereas medium-element meshes were applied to rock layers (Fig. 4). Because only the residual soil layer was substantially influenced by rainfall infiltration, the aforementioned applied mesh densities ensured accurate modeling results and reduced computational cost and time.

Hydraulic and mechanical boundary conditions prescribed in the model slopes are also illustrated in Fig. 4. The standard fixity was applied as the mechanical boundary; the two lateral boundaries were allowed to move only in the vertical directions whereas the bottom

Table 2
Input parameters for hardening soil mode for residual soil layer.

Property	Values	
	Slope 1	Slope 2
<i>Stiffness properties</i>		
E_{50}^{ref} , secant modulus (kPa)	13,750	15,130
E_{95}^{ref} , tangent oedometer loading modulus (kPa)	9625 ^a	10590 ^a
E_{ur}^{ref} , unloading-reloading modulus (kPa)	41250 ^b	45380 ^b
ν_{ur} , unloading-reloading Poisson's ratio	0.3	0.3
m , modulus exponent	0.5	0.5
R_f , failure ratio	0.9	0.9
<i>Strength properties</i>		
ϕ' , friction angle (degree)	27	30
c' , cohesion (kPa)	6	10
ψ , dilation angle (degree)	0 ^c	0 ^c
<i>Bulk unit weight</i>		
γ_{unsat} , unsaturated unit weight (kN/m ³)	19.5	19.5
γ_{sat} , saturated unit weight (kN/m ³)	20.1	20.1

^a Assumed to be $0.7E_{50}^{ref}$ as the default value in PLAXIS.

^b Assumed to be $3E_{50}^{ref}$ as the default value in PLAXIS.

^c Estimated by $\psi = \phi - 30^\circ$ (Bolton, 1986).

boundary was restrained from movement. Examination of the developed stress levels in the numerical models revealed that the assumed mechanical boundary conditions were appropriate.

Hydraulic boundaries at two lateral ends were initially set to be constant head boundary conditions on the basis of the monitored GWT levels. During the analysis, the hydraulic boundaries were switched to seepage boundary conditions to enable variations in GWT levels because of wetting and drying cycles. Downward vertical influx was prescribed on the slope surface to model rainfall, whereas upward influx was imposed on the surface boundary to simulate evapotranspiration. The input values of downward flux during rainfall were obtained from the actual rainfall records from the nearest precipitation measuring station. The value of upward flux on dry days was estimated to be 10 mm/day based on studies on the average evapotranspiration rate of mountain areas in Taipei City (Chen et al., 2005; Hsu et al., 2006; Kao et al., 2012). The effect of evapotranspiration on soil moisture was not considered during rainfall because of the presence of surface water and associated high humidity. The hourly data of infiltration and evapotranspiration were used as the prescribed input flux. Surficial water run-off was permitted when the developed PWP on the slope surface changed to a positive value.

4.2. Initial conditions

The initial stress within the soil body of the slope was generated using the PLAXIS gravity loading function for nonhorizontal surfaces and soil stratifications. For gravity loading, the initial stress was established by applying the soil self-weight during the first calculation phase and solving for equilibrium. The initial PWP was generated by conducting a transient seepage analysis. The value of modeling antecedent hydrological conditions on any subsequent hydrology modeling has been highlighted by Blake et al. (2003), Oh and Lu (2015), Qi and Vanapalli (2015), and Yoo and Jung (2006).

For Slope 1, a small, prescribed flux was specified at the top of the slope model for a considerable time until steady state conditions were reached. The quantities of the prescribed flux were adjusted until the calculated initial matric suction value fell within the range of monitored field sections. Fig. 3 displays the locations of matric suction measured using tensiometers. The measured field suction values range from 50 to 80 kPa at various depths of 0.3–1.5 m from the slope surface. For

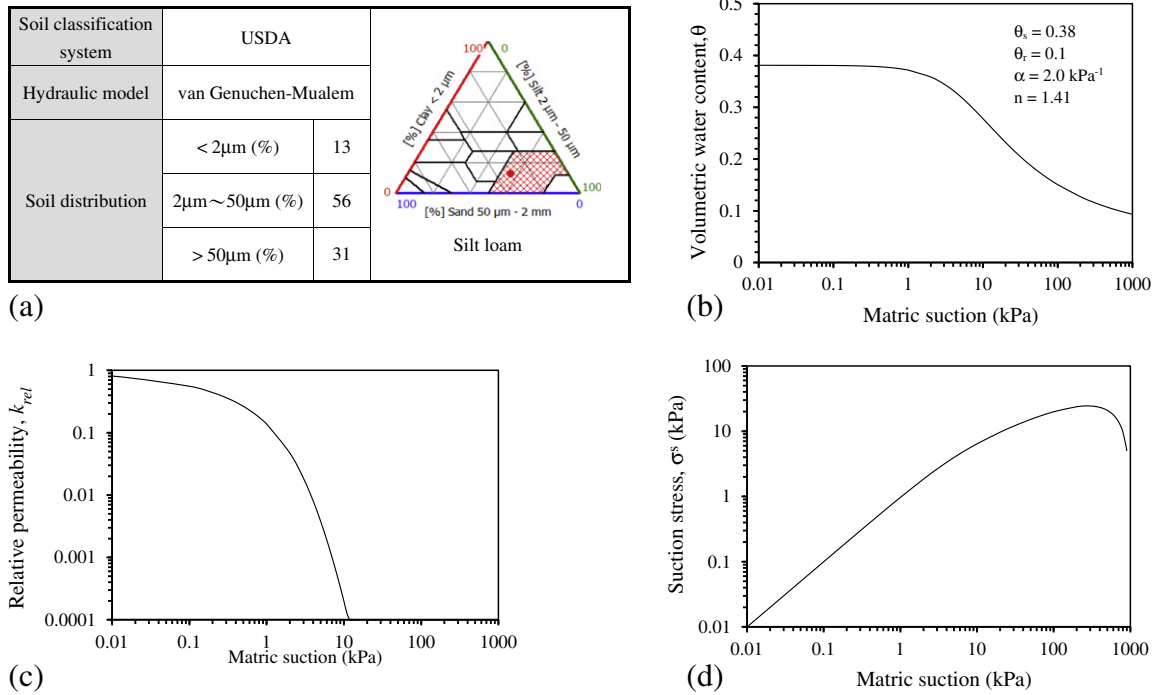


Fig. 5. Residual soil hydraulic properties: (a) soil particle distribution; (b) soil water characteristic curve (SWCC); (c) hydraulic conductivity function curve; (d) suction stress characteristic curve (SSCC).

Slope 2, because the simulated year (2012) was much wetter than the year (2008) when suction was measured, transient seepage analysis was performed for one month using the actual rainfall data from January 2012 to establish initial hydrology conditions.

4.3. Material properties

Table 1 summarizes the input soil and rock properties used in the present study. Residual soil was modeled as a stress-dependent, hyperbolic, elastoplastic material by using the Hardening Soil model (Schanz et al., 1999) and was analyzed using effective stress parameters under

drained conditions. Table 2 lists the input soil parameters of the Hardening Soil model. Fig. 5 illustrates the unsaturated hydraulic properties of the residual soil. Unlike the Barcelona Basic model (Alonso et al., 1990) in PLAXIS which uses effective stress and suction as two state variables, the Hardening Soil model only uses generalized effective stress as the main state variable and cannot separately account for the strain increments associated with changes in effective stress and suction. In other words, the Hardening Soil model implicitly assumes strain increments induced by the changes of loading and suction are equivalent. This assumption was considered valid for the presented case study because the residual soil exhibited a low suction range (<80 kPa).

The effective soil shear strength properties of the residual soil in Slopes 1 and 2 were determined from direct shear tests on undisturbed soil samples from the site investigation program. The effect of soil dilatancy was not considered in the simulation because the soil dilation angle ψ , is negligible based on the empirical relationship $\psi = \phi - 30^\circ$ proposed by Bolton (1986). The initial soil modulus E_i was estimated using the empirical correlation, which involves the related secant soil modulus being subject to the standard penetration test (SPT) N value, as suggested by Schmertmann (1970) and Kulhawy and Mayne (1990).

$$E_i = \alpha_f p_a N_{60} \tag{11}$$

where α_f is the coefficient to account for fine content ($\alpha_f = 5$ was used for sands with fines); p_a is one atmospheric pressure; and N_{60} is the corrected SPT-N value. The calculated E_i values were further converted to the soil moduli at 50% of the stress level (E_{50}) by using Eq. (12), in which a default failure ratio R_f value of 0.9 was used.

$$E_{50} = E_i \frac{2 - R_f}{2} \tag{12}$$

As indicated in Table 1, the soil moduli estimated by Eqs. (11) and (12) are 5651 and 7800 kPa for Slopes 1 and 2, respectively. The estimated soil moduli fall within the normal range of soil modulus in this area (Yang et al., 2016a, 2016b).

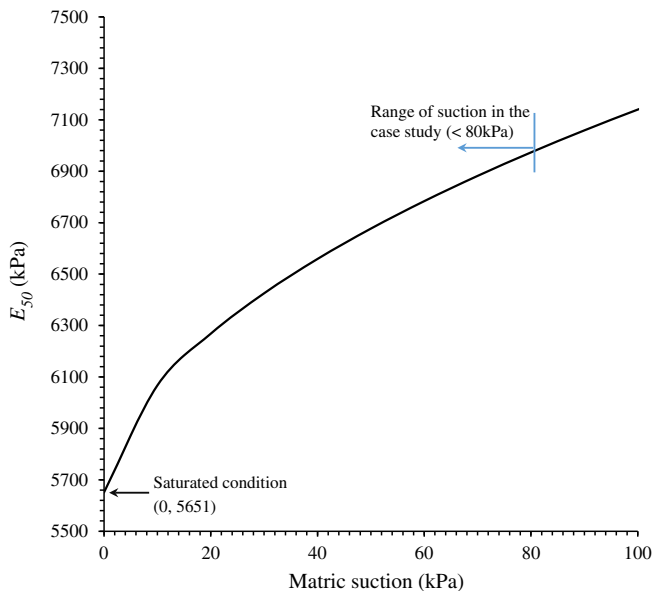
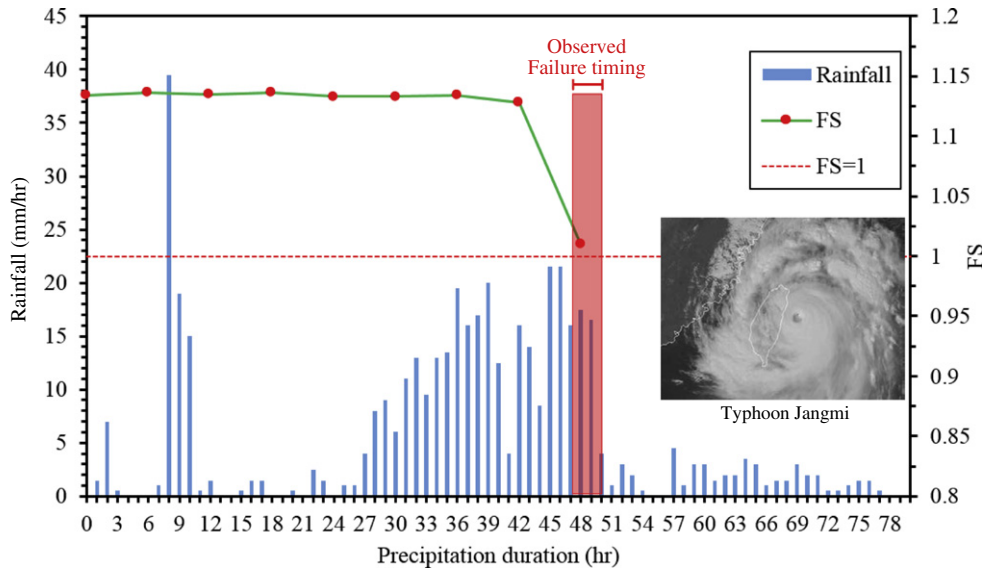
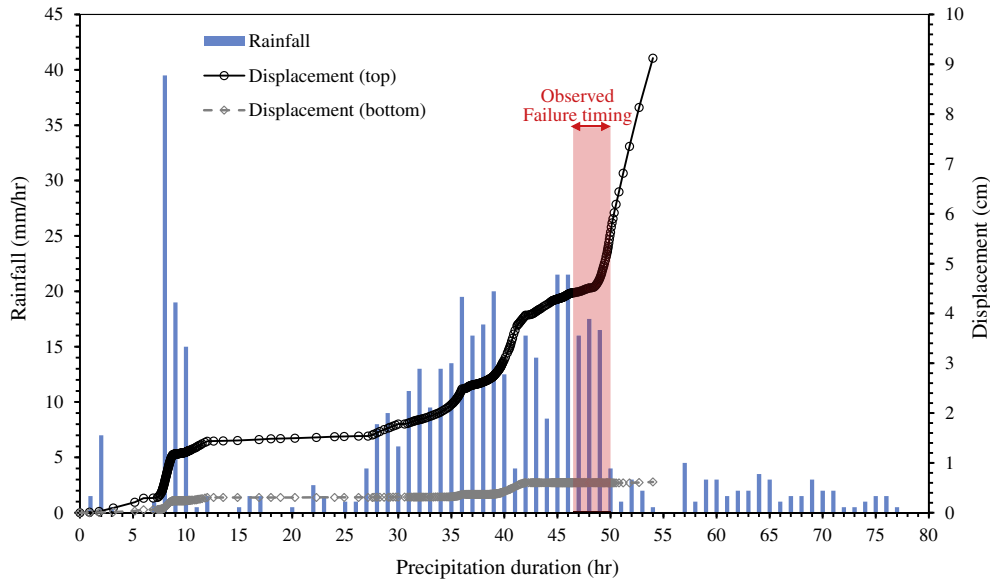


Fig. 6. Variation of soil modulus with respect to suction.



(a) factor of safety



(b) slope displacement

Fig. 7. Model validation of Slope 1: (a) factor of safety; (b) slope displacement.

Thereafter, the value of reference modulus E_{50}^{ref} in Hardening Soil model was determined:

$$E_{50} = E_{50}^{ref} \left(\frac{c' \cos \phi' + \sigma_3' \sin \phi'}{c' \cos \phi' + p^{ref} \sin \phi'} \right)^m \quad (13)$$

where E_{50} is the soil modulus at 50% stress level; p^{ref} is the reference stress ($= 1 \text{ atm} = 101.3 \text{ kPa}$); c' and ϕ' are the effective cohesion and friction angle; and σ_3' is the effective minor principal stress at mid-height of the residual soil layer.

Compared with Mohr-Coulomb model, the main reason of selecting Hardening Soil model is twofold. First, a nonlinear (hyperbolic) stress-strain relation is modeled in Hardening Soil model, while a linear elastic stress-strain relation is used in Mohr-Coulomb model. The nonlinear stress-strain relation in Hardening Soil model can effectively model the changes of soil modulus with different stress levels, which can better simulate soil deformation at large soil strain conditions (e.g., the case

in Slope 2). Second, a stress-dependent soil modulus, meaning it changes as effective stress changes, is modeled in Hardening Soil model, while a constant (stress-independent) soil modulus is used in Mohr-Coulomb model. The stress-dependent modulus is an essential feature to better describe changes in soil modulus with matric suction for modeling unsaturated soil behavior. Fig. 6 displays the numerical relationships between the soil modulus and matric suction as predicted by Eq. (13).

In regard to the hydraulic properties of soil, soil-saturated vertical hydraulic conductivity ($k_{s,v}$) was determined from a field permeability test (Fig. 3) at a depth of 0.1–0.5 m by using the Guelph permeameter (GP), a portable field instrument. The applications of the Guelph permeameter were thoroughly discussed by Hayashi and Quinton (2004), Reynolds et al. (1985), and Reynolds et al. (1984). Soil saturated horizontal hydraulic conductivity ($k_{s,h}$) was assumed to be 1.5 times $k_{s,v}$ to account for the effect of stratified soil deposits. The soil water characteristic curve (SWCC) of the residual soil (Fig. 5b) was estimated according to the particle size distribution as classified by the USDA soil

classification system (Fig. 5a). The predicted SWCC of the residual soil exhibited an air entry value of $\psi \approx 3$ kPa and the fitting parameters: $\theta_s = 0.38$, $\theta_r = 0.1$, $\alpha = 2 \text{ kPa}^{-1}$, and $n = 1.41$. The relative hydraulic conductivity k_{rel} (Fig. 5c) of the k -function curve was established using Eq. (4) according to the measured saturated hydraulic conductivity value and the curve fitting parameters in the SWCC. The suction stress characteristic curve (SSCC) was obtained using Eq. (8) (Fig. 5d). Within the suction range in this study (<80 kPa), suction stress increases as the matric suction increases (Fig. 5d).

The rock layers were modeled as linear, elastic-perfectly plastic materials by using the Mohr–Coulomb model and were analyzed using saturated, total stress properties under undrained conditions. Saturated conditions for rock layers were selected for two reasons: (1) the primary sections of rock layers are submerged under the GWT; (2) the unsaturated seepage flow displays a limited impact on the rock layer because of the relatively low permeability of rock layers. The shear strengths (i.e., cohesions) of rock layers were calculated from the measured uniaxial compression strength (q_u). The rock moduli and saturated hydraulic conductivities were estimated according to the properties of similar rock types suggested by Goodman (1989).

5. Results and discussion of Slope 1 (failure case)

5.1. Model validation

Fig. 7 shows model validation for the failure of Slope 1 during Typhoon Jangmi in 2008 by comparing the predicted and observed failure timing. Fig. 7a depicts the variation of the FS during a 48-hour rainfall period that was computed using the ϕ/c reduction function in PLAXIS. In the ϕ/c reduction approach, the strength parameters $\tan\phi$ and c of the soil are successively adjusted until the slope approaches the verge of failure. The FS is computed as follows:

$$FS = \sum M_{sf} = \frac{\tan \phi_{input}}{\tan \phi_{adjusted}} = \frac{c_{input}}{c_{adjusted}} \quad (14)$$

where $\sum M_{sf}$ is the total multiplier defined in PLAXIS manual (Brinkgreve et al., 2015). The value of $\sum M_{sf}$ is equivalent to the value of FS; ϕ_{input} and c_{input} are the original input soil strength properties and $\phi_{adjusted}$ and $c_{adjusted}$ are the adjusted soil strength properties calculated during the ϕ/c reduction analysis. Notably, the definition of FS in Eq. (14) can be perceived as the ratio of available soil shear strength to the mobilized shear stress required for equilibrium, which is identical to the definition of FS in the conventional limit equilibrium analysis with rigorous slice methods.

In Fig. 7a, the FS gradually decreased with rainfall until $t = 42$ h and thereafter the FS rapidly decreased from a value of 1.13 to 1.0 from $t = 42$ to 48 h. The rapid decrease of FS indicates that the downward wetting front arrived at the depth of critical failure surface. Predicted displacement (Fig. 7b) at the top (300 mm below slope surface) of the residual soil layer gradually increased with rainfall and sudden rapid movement occurred after 42 h. The bottom (300 mm above soil-rock interface) of the residual soil layer exhibited relatively little movement. Although there is no increase in degree of saturation at the bottom of the residual, the soil deformation at the bottom was driven by the soil deformation-induced shear stress on the top. The observed predicted timing for the rapid decrease of FS and increasing displacement correlates positively with the observed failure timing as indicated in Fig. 7; as a result, it was confirmed that the developed hydro-mechanical model is capable of accurately predicting the timing of torrential rainfall-induced slope failure. Fig. 8 shows incremental displacement vectors at the moment of failure and the displacement vectors can be clearly observed along the slope surface at a shallow depth.

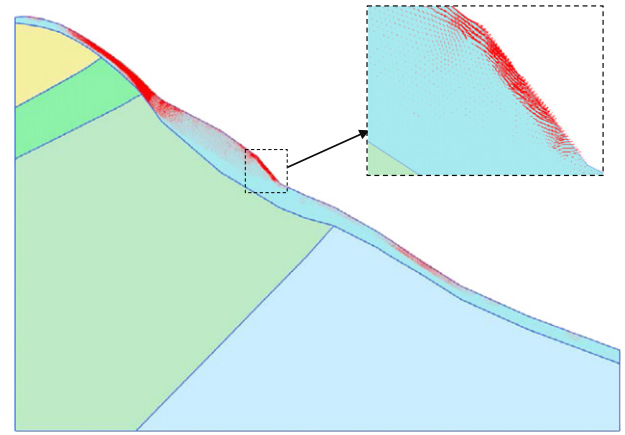


Fig. 8. Incremental displacement vectors of Slope 1 at $t = 42$ h.

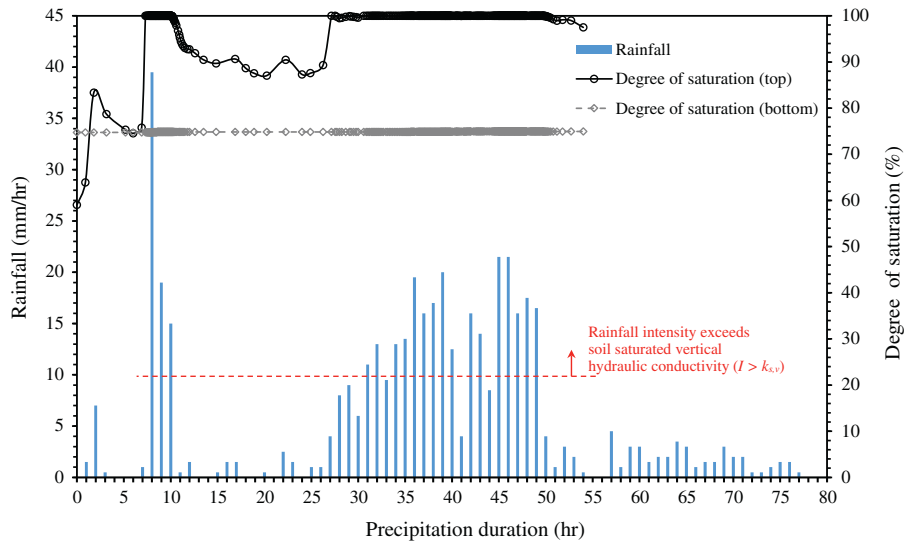
5.2. Hydrological response and failure mechanism

After the model was validated, the hydrological response within the slope model extracted from the numerical simulation (Fig. 9) was examined to provide insight on stress information and the triggering failure mechanism. Fig. 9 displays the variation of degree of saturation (S), PWP, and suction stress at the top (300 mm below slope surface) and bottom (300 mm above soil-rock interface) of the residual soil layer. Because the hydraulic conductivity of the residual soil limited the maximum amount of water that can infiltrate the soil, the changes in S were pertinent to the relationships between rainfall intensity I and vertical saturated hydraulic conductivity of the residual soil $k_{s,v}$. When I exceeded $k_{s,v}$ ($2.76 \times 10^{-4} \text{ cm/s} = 9.94 \text{ mm/h}$), the soil at the top became fully saturated ($S = 100\%$) and runoff occurred along the slope surface. However, surficial water ponding was not allowed in the simulation because of runoff considerations. By contrast, when rainfall intensity was lower than $k_{s,v}$, the soil S increased when infiltration progressed but the soil was not fully saturated at the arrival of the wetting front. Fig. 9a also displays no change of S at the bottom of the residual soil layer, suggesting that the wetting front did not reach the bottom of the residual soil within the short typhoon period.

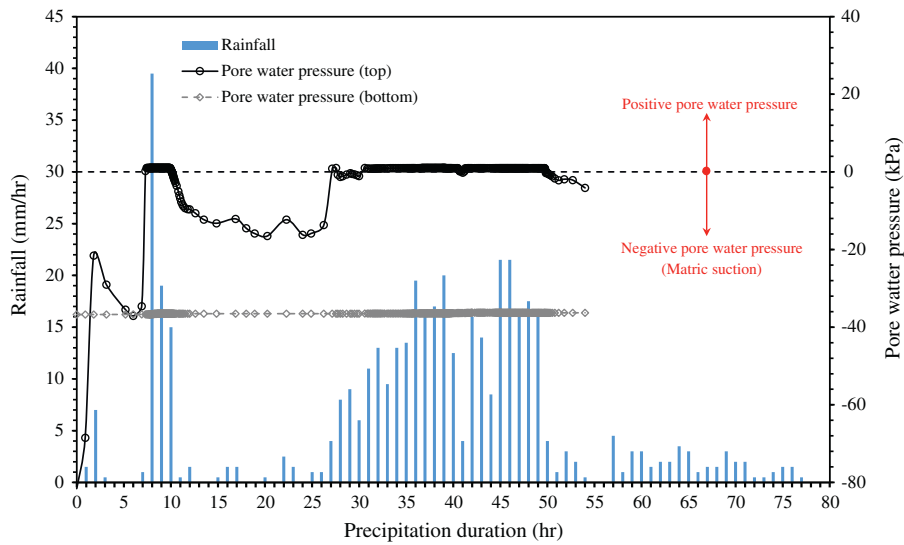
Fig. 9b and c depict the variation of PWP and suction stress, respectively. Notably, the negative PWP in Fig. 9b is equal to the matric suction and the positive suction stress in Fig. 9c is equivalent to the positive PWP because $\Theta = 1$ at $S = 100\%$. The numerical results indicate the matric suction fully lost at the top of the residual soil layer and positive PWP (≈ 1 kPa) developed, resulting in the decrease of effective stress at the top, ultimately causing the slope failure. Because the wetting front did not reach the bottom of the residual soil layer during the typhoon period (Fig. 9a), PWP and suction stress within the soil at the bottom remained unaltered. Based on the hydrological information and failure mechanism discussed previously, the failure of Slope 1 was concluded to be a rainfall-induced shallow slope failure (within a 2-m depth from the top). After learning the failure mechanism from the numerical study, remediation measures that employ slope surface protection combined with a surface drainage/discharge system (Fig. 2b) are recommended to reduce infiltration, control soil erosion, and improve slope surface stability.

5.3. Stress path

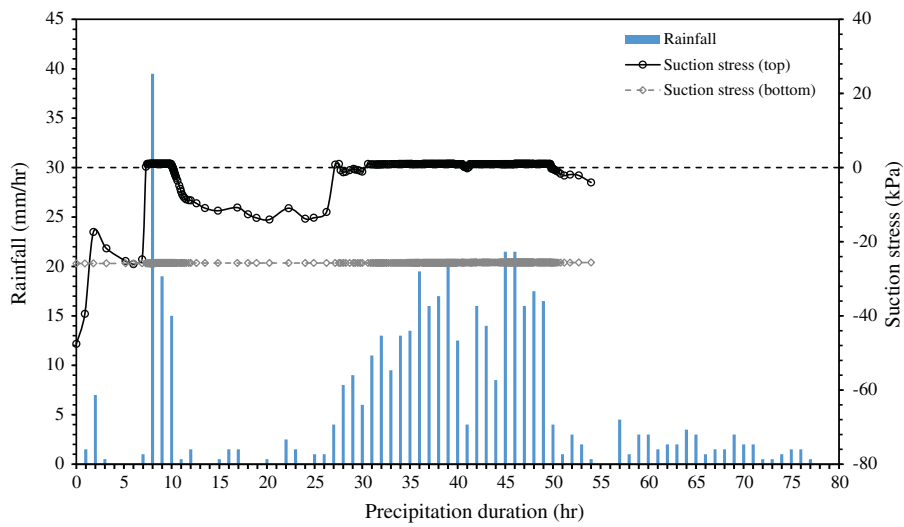
Fig. 10 illustrates the two- and three-dimensional stress paths (based on the MIT stress-path approach) for soil at a 2-m depth from the slope surface subject to rainfall infiltration during Typhoon Jangmi. Fig. 10a displays the three-dimensional stress path with a net total stress p , matric suction $u_a - u_w$, deviatoric stress q space, and the conventional



(a) degree of saturation



(b) pore water pressure



(c) suction stress

Fig. 9. Simulation results of Slope 1: (a) degree of saturation; (b) pore water pressure; (c) suction stress.

extended Mohr–Coulomb envelope. The three-dimensional stress path in Fig. 10a is presented as a two-dimensional space (in a net effective stress p' and deviatoric stress q space) in Fig. 10b according to the generalized effective stress principle as defined in Eqs. (5) and (7). In Fig. 10b, the three-dimensional extended Mohr–Coulomb envelope was transformed into a unified failure envelope (i.e., K_f line). The use of the generalized effective stress principle for unsaturated soil enables a clear presentation of the stress path and unified failure envelope in the p' - q space.

Fig. 10b indicates that before the arrival of the wetting front ($t < 42$ h), the soil stress path was spinning; the movement of the stress path is attributable to the migration of the initial soil moisture driven by gravity. When the wetting front arrived, a loss of matric suction caused the negative suction stress within the soil to decrease, causing the net effective stress to decrease. In addition, decrease of the deviatoric stress q was also observed in the stress path during rainfall infiltration. It is

likely due to the fact that the overburden pressure decreased as the soil deformed downslope. The soil stress path, therefore, moved to the lower left in the p' - q space, signifying that the soil effective stress decreased as infiltration progressed, and eventually the soil stress path contacted the K_f line at the limit state, indicating the failure of the slope.

6. Results and discussion of Slope 2 (excessive deformation case)

6.1. Model validation

Fig. 11 displays the model validation of Slope 2 that compared the measured and predicted slope displacement at the inclinometer location indicated in Fig. 4b. The analysis for Slope 2 was performed for a year-long duration in 2012: the recorded hourly rainfall on rainy days and average daily evapotranspiration rate of 10 mm/day on dry days were specified as the input flux. Because the actual rainfall data in January 2012 was applied to establish initial hydrology conditions, the numerical results present conditions occurring after February 2012. In the present study, eight rainfall events were selected according to the criteria of rainfall intensity of $I \geq 50$ mm/day as the red line indicated in Fig. 12. Four of these rainfall events were influenced by typhoons (Typhoons Talim, Saola, Tembin, and Jelawat). Table 3 summarizes the basic precipitation information of the eight rainfall events in 2012.

Fig. 11 illustrates the measured and predicted slope displacement over time at the slope top in 2012. The developed hydro-mechanical model effectively captured the increasing trend of slope displacement. The predicted total displacement (= 7 mm) in 2012 is approximate to the measured total displacement (= 8.5 mm) from inclinometer readings. The precision of inclinometer is ± 0.2 mm per meter. Considering that the residual soil of Slope 2 is 2 m deep at slope crest, the expected accumulated error of the inclinometer reading is ± 0.4 mm, which is only attributed to 4% error (= 0.4 mm/8.5 mm) of the measured total displacement. The numerical results revealed that substantial plastic deformation of the slope occurred and was associated with high-intensity rainfalls (Events 3 and 5) or long durations (Events 2 and 8), which corresponds to the total amount of water volume entering into the soil. The effect of the soil modulus on the predicted displacement was evaluated by reducing the E_{50} value by 20%. The comparative result indicated that the discrepancy between two predicted results was insignificant before May, but the difference increased when the plastic deformation developed during high-intensity rainfalls (Events 3 and 5) or long durations (Events 2 and 8). At the end of the simulation, the predicted displacement increased up to approximately 20% when the lower E_{50} value was input.

Fig. 12 displays the variation of the FS of the slope under drying and wetting cycles. The FS of the slope dropped at each rainfall event and recovered during dry days because of the effect of modeling evapotranspiration. The values of the FS varied approximately between 1.4 and 1.1. Although the slope still exhibited a FS > 1.0 , the low FS value and increasing slope displacement suggested that the slope approached unstable conditions during rainfall.

6.2. Hydrological response and deformation mechanism

Fig. 13 displays the variation of degree of saturation, PWP, and suction stress at the top and bottom of the residual soil layer at the inclinometer location. The numerical results indicated that the S at the top residual soil reacted immediately to wetting and drying cycles, resulting in a sharp fluctuation in the S . In contrast to the top residual soil, a delay in soil moisture changes at the bottom of the soil layer was observed. The variation in the degree of saturation was therefore relatively smooth. After rainfall events, residual soil at the bottom became fully saturated and remained fully saturated for a considerable time. Because of the low permeability of the rock layers preventing water from

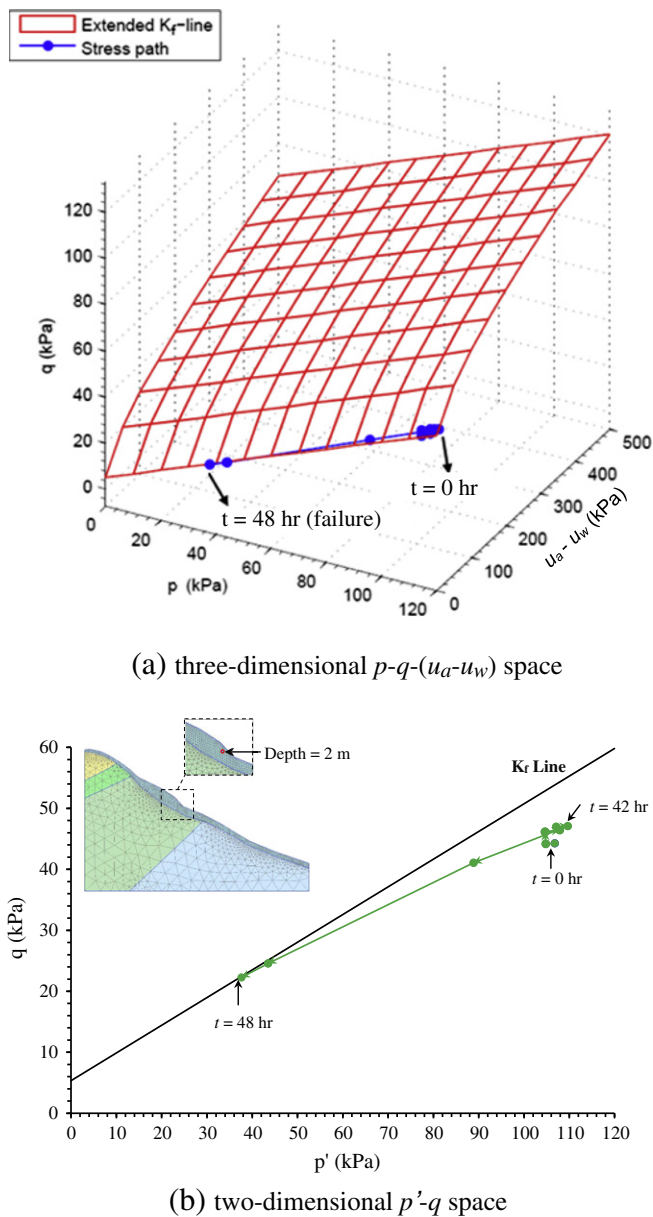


Fig. 10. Stress path of soil at the depth of 2 m from slope surface subject to infiltration (0–48 h): (a) three-dimensional p - q - $(u_a - u_w)$ space; (b) two-dimensional p' - q space.

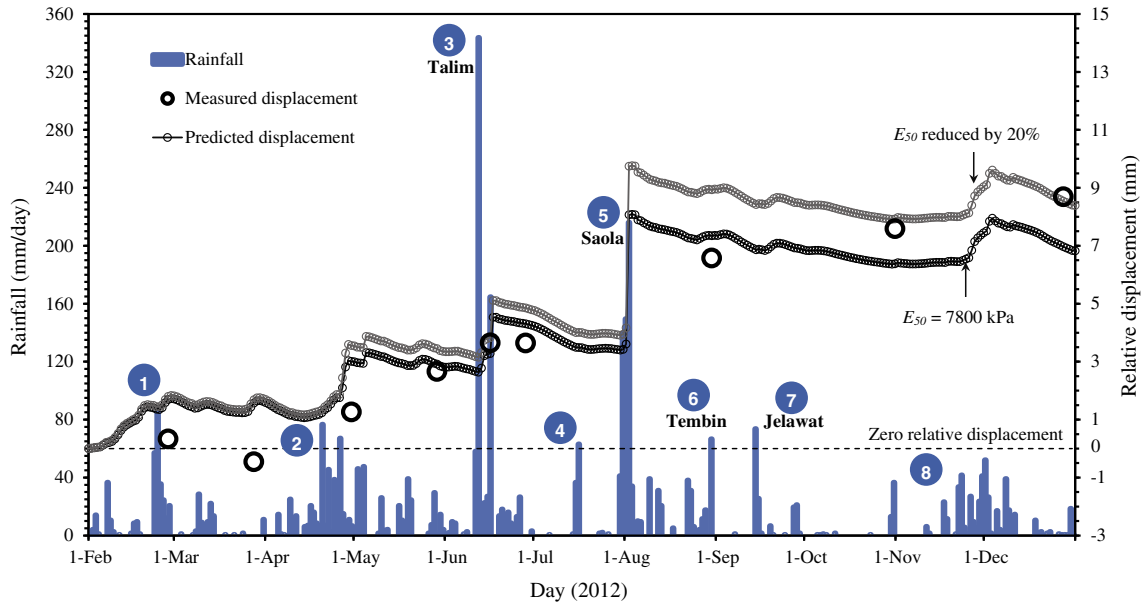


Fig. 11. Model validation of Slope 2 by comparing measured and predicted displacement at location of inclinometer.

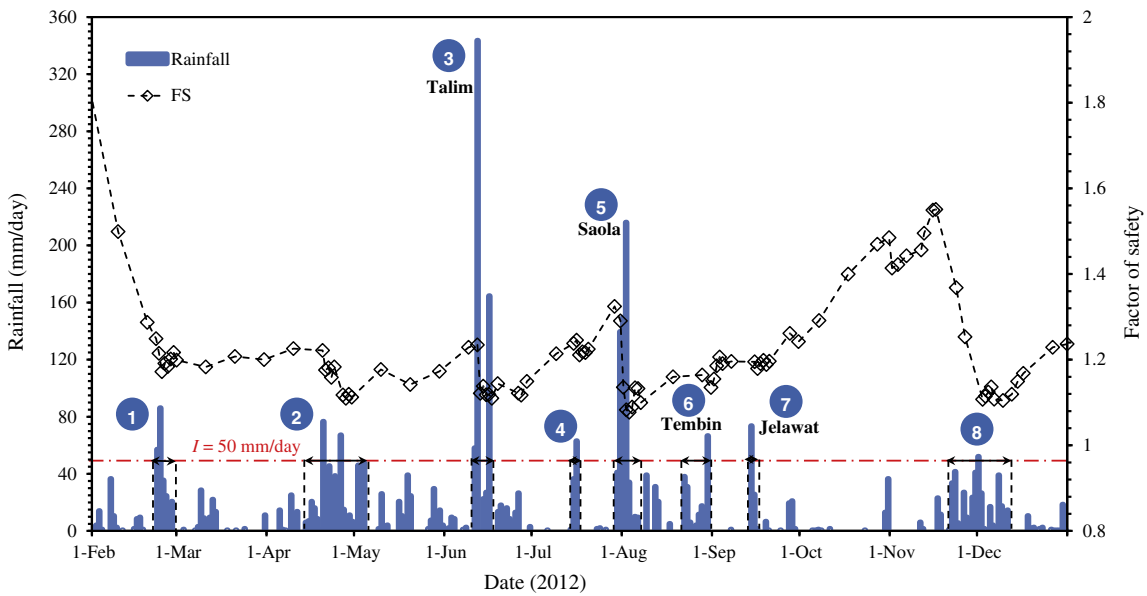


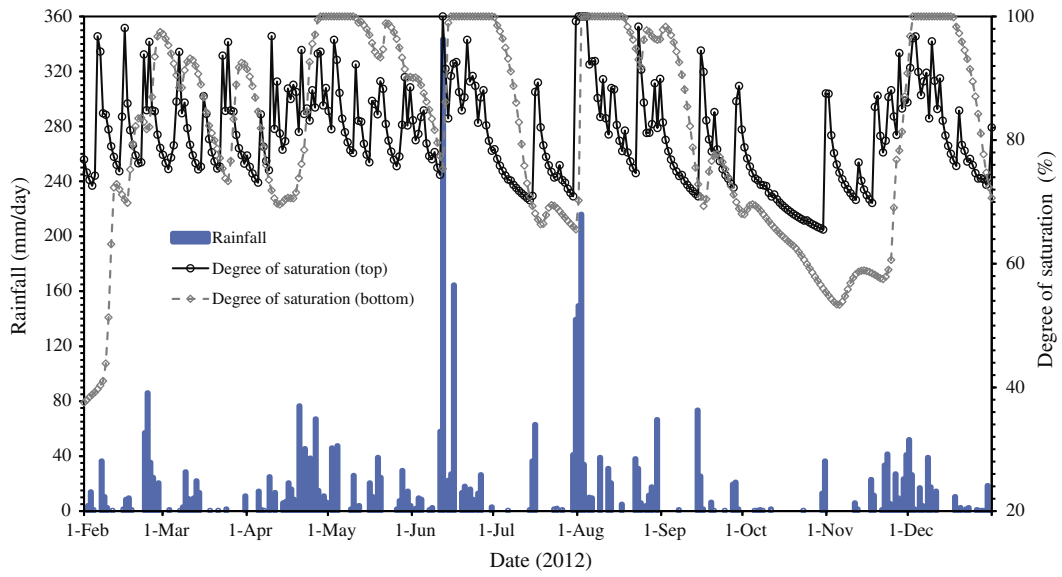
Fig. 12. Predicted factor of safety with time.

infiltrating further, positive PWP developed at the soil–rock interface at the bottom of the residual soil layer (Fig. 13b). The maximum PWP reached $u_w = 15$ kPa at Event 5 and around $u_w = 10$ kPa at Events 2, 3, and 8.

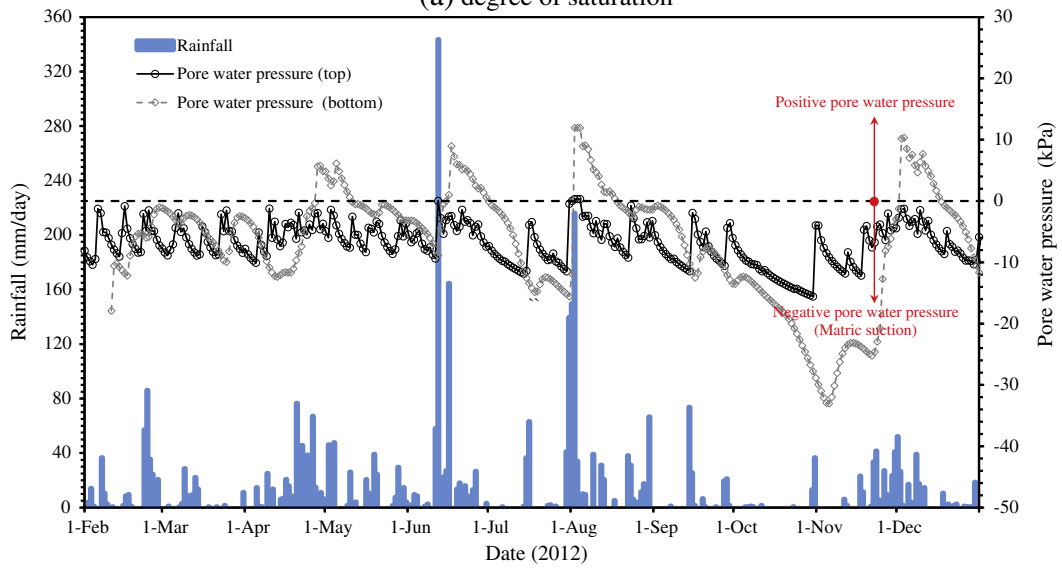
Fig. 13c also indicated similar trends in suction stress variation. Because the top residual soil remained unsaturated, nearly no positive suction stress developed at the top. However, negative suction stresses at the bottom decreased considerably and positive suction stresses

Table 3
Rainfall events in Year 2012.

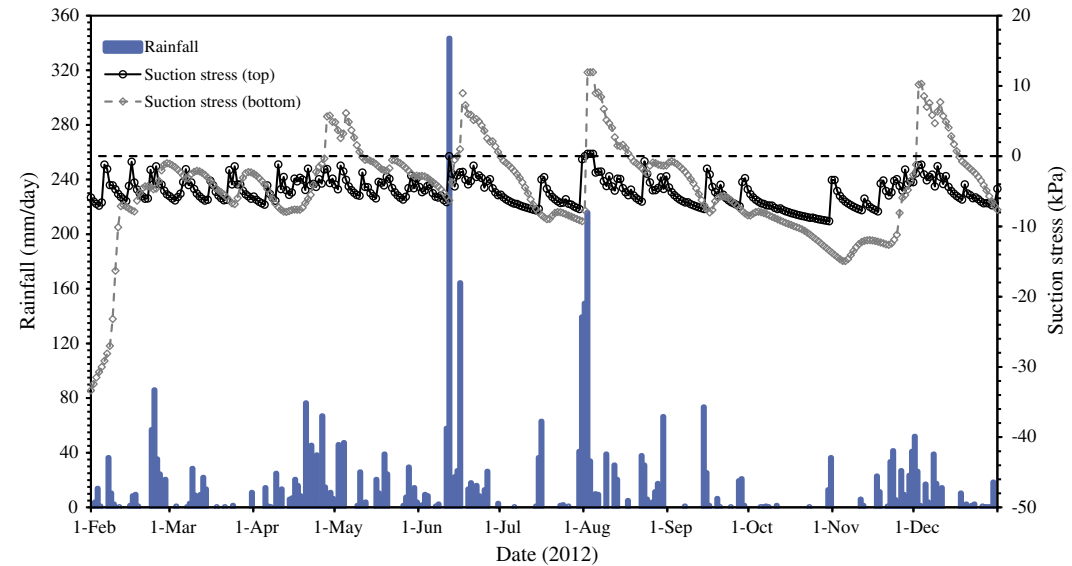
Event number	Date	Duration (day)	Maximum 24-hour rainfall (mm/day)	Cumulative rainfall up to maximum rainfall (mm)	Total cumulative rainfall (mm)
1	February 23–28	6	86	143	235.5
2	April 14–May 4	21	76.5	135	435
3	June 11–16 (Typhoon Talim)	6	343.5	401.5	615
4	July 14–16	3	63	37.5	100.5
5	July 31–August 6 (Typhoon Saola)	7	216	505	558.5
6	August 22–30 (Typhoon Tembin)	9	66.5	174.5	174.5
7	September 14–16 (Typhoon Jelawat)	3	73.5	73.5	100
8	November 21–December 11	21	52	240.5	360.5



(a) degree of saturation



(b) pore water pressure



(c) suction stress

Fig. 13. Simulated results of Slope 2: (a) degree of saturation; (b) pore water pressure; (c) suction stress.

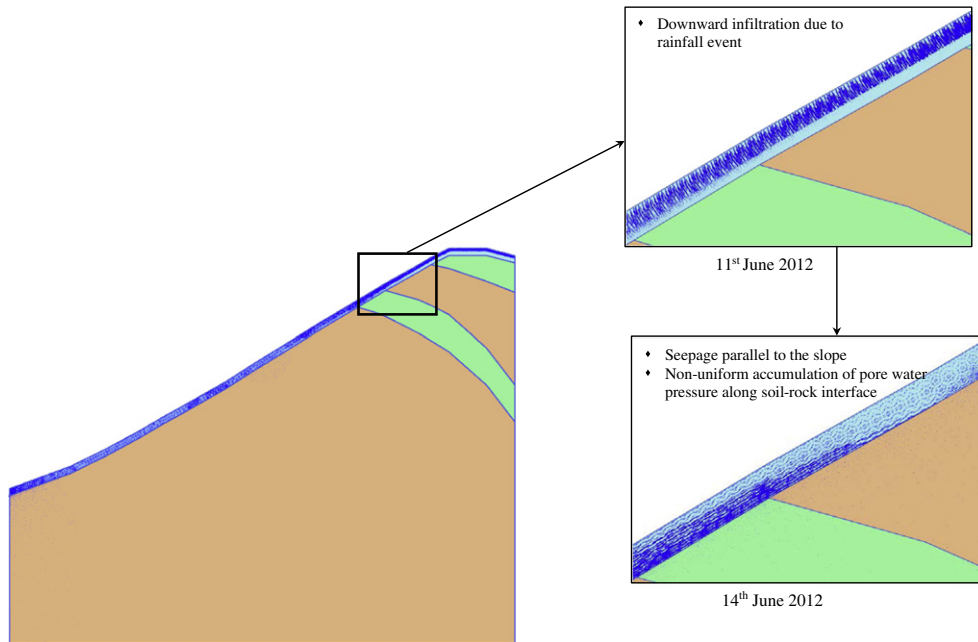


Fig. 14. Seepage vectors in Slope 2.

(i.e., positive PWP) developed after major rainfall events. Therefore, effective stress decreased because of a loss of negative suction stress. The negative suction stress could possibly recover following the dry days.

Fig. 14 shows the predicted seepage discharge vectors at the onset of Event 3 on June 11, 2012 and after the wetting front reached the soil–rock interface on June 14, 2012. A downward rainfall infiltration-induced seepage flow was observed at the onset of rainfall. After the wetting front reached the soil–rock interface, water remained at the interface and a lateral seepage flow subsequently developed parallel to the interface. The height of seepage flow increased from the upper to the lower slope, leading to a nonuniform accumulation of PWP along the soil–rock interface. Inspection of the numerical results indicated that the positive PWP likely developed at the middle and bottom sections of the slope whereas the PWP at the top sections of the slope remained negative during major rainfall events (Table 4).

Based on the preceding discussion, the deformation of Slope 2 was caused by the positive PWP accumulation at the bottom of the residual soil layer along the soil–rock interface. Remediation measures involving subsurface drainage (e.g., horizontal drains and relief wells) in conjunction with surface drainage are advised to reduce future rainfall percolation and facilitate excessive PWP dissipation. Additionally, soil reinforcement techniques such as soil nails, anchors, or micropiles can be installed to enhance slope stability.

Table 4

Maximum suction stress and pore water pressure at the soil–rock interface for each rainfall event.

Rainfall event	Date (year 2012)	Suction stress (kPa)			Pore water pressure (kPa)		
		Top	Middle	Bottom	Top	Middle	Bottom
1	February 24	−12.60	12.69	14.01	−27.31	12.69	14.01
2	April 27	2.02	12.72	14.02	2.02	12.72	14.02
3	June 16	5.46	12.72	14.02	5.46	12.72	14.02
4	July 16	−19.25	11.44	14.01	−59.64	11.44	14.01
5	August 2	12.82	12.72	14.02	12.82	12.72	14.02
6	August 30	−8.64	12.71	14.01	−14.34	12.71	14.01
7	September 14	−17.54	12.48	14.01	−50.16	12.48	14.01
8	December 1	5.09	12.72	14.02	5.09	12.72	14.02

6.3. Stress path

Fig. 15 depicts the selected stress path of soil at a 2-m depth, subject to drying and wetting cycles for three months (September to December). On dry days, the soil stress path moved to the right, indicating that net effective stress increased because matric suction and negative suction stress increased. On rainy days, the soil stress path moved to the left because of the decrease of soil effective stress induced by the decrease in matric suction and negative suction stress. Because the variation of suction stress affected both major and minor principle stresses, the deviatoric stress q was not influenced by the variation of suction stress. The stress path moved parallel to the p' axis under drying and wetting cycles, but did not contact the K_f line.

6.4. Relationship between the slope FS and rainfall

The relationships between slope FS and the corresponding hydrological data (i.e., rainfall and soil PWP) were examined and are discussed in this section. Table 3 summarizes the hydrological data including the maximum 24-hour rainfall, cumulative rainfall up to the maximum 24-hour rainfall, and total cumulative rainfall for the eight selected rainfall events. Fig. 16a displays the correlation of the maximum 24-hour rainfall with the corresponding minimum FS for each rainfall event. In general, no clear correlation between the maximum 24-hour rainfall and the corresponding FS was observed (Fig. 16a).

Because suction stress is dependent on matric suction (Fig. 5d), the slope antecedent hydrological conditions prior to the maximum 24-hour rainfall affected the state of soil effective stress during rainfall events. To consider this effect, the data points in Fig. 16a are categorized by the number of rainy/wetting days prior to the maximum 24-hour precipitation. After categorization, the relationship between the maximum 24-hour rainfall and the corresponding FS shifts with the number of wetting days prior to the maximum 24-hour precipitation. At the same maximum 24-hour rainfall, the rainfall event with fewer prior wetting days, likely exhibiting higher matric suction (and suction stress), leads to a higher FS. For example, when comparing Events 4 and 6 which have similar maximum 24-hour precipitation value, Event 4, which has fewer prior wetting days (i.e., 1 day), exhibits an FS higher than that of Event 6 (8 prior wetting days).

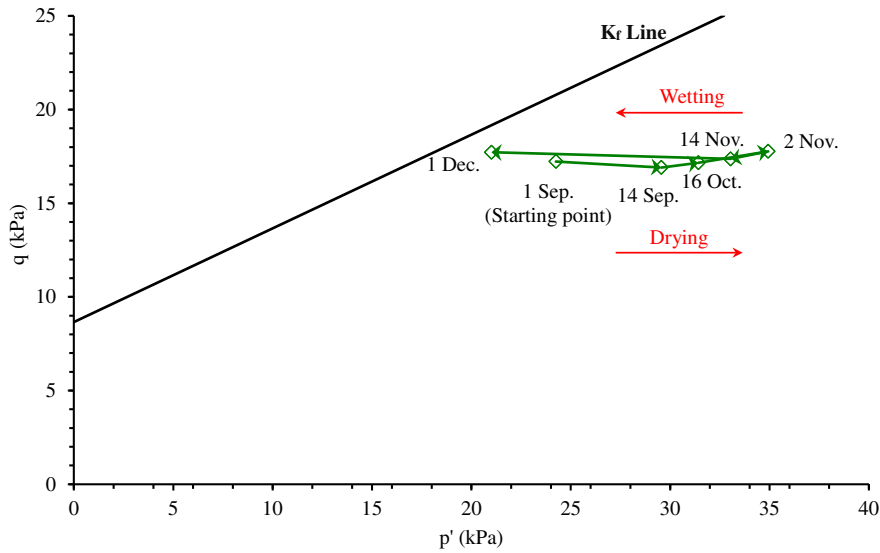


Fig. 15. Stress path of soil at the depth of 2 m from slope surface subject to drying and wetting cycle (September–December 2012).

To account for the slope antecedent hydrological conditions, the relationship between the minimum FS and the cumulative rainfall for each rainfall event is established in Fig. 16b. Fig. 16b displays that the slope of the FS decreased linearly with an increase in cumulative rainfall. When the cumulative rainfall up to the maximum 24-hour rainfall or the total cumulative rainfall in one rainfall event was applied, a positive correlation with the FS slope was

observed. This study demonstrated that the cumulative rainfall is a suitable indicator for slope stability when its relationship with the FS has been established.

6.5. Comparison between finite element and infinite slope analysis

Residual slopes underlain by a low permeable bedrock often exhibit a surficial infinite slope failure (Rahardjo et al., 1995). Therefore, the FSs of Slope 2 under the eight selected rainfall events were also analyzed using the infinite slope equation based on the generalized effective stress principle:

$$FS = \frac{c' + \sigma' \tan \phi'}{\gamma H \cos \beta \sin \beta} = \frac{c' + [(\sigma - u_a) + \theta(u_a - u_w)] \tan \phi'}{\gamma H \cos \beta \sin \beta} \quad (15)$$

where H is the depth of the sliding plane; β is the slope angle; other parameters have been defined previously. Because the PWP was nonuniformly distributed along the slope as discussed previously (Table 4), the values of suction stress $-\theta(u_a - u_w)$ in Eq. (15) were adopted from the FE analyses of Slope 2 at the soil–rock interface at three different locations: the top, middle, and bottom sections (Fig. 17).

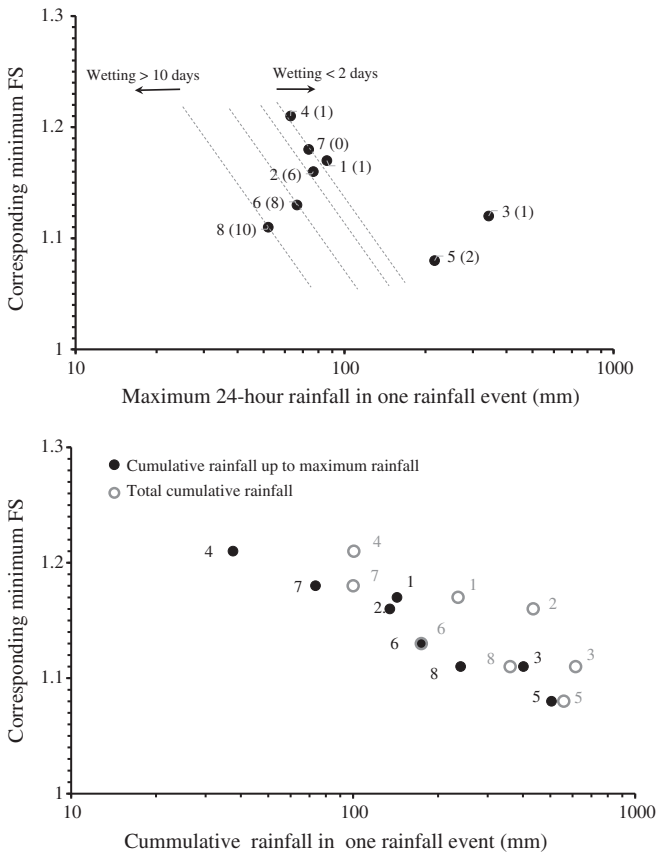


Fig. 16. FS vs. rainfall relationship: (a) maximum 24-hour rainfall; (b) cumulative rainfall (numbers indicate the rainfall event number; values in parenthesis indicate number of wetting days prior to maximum precipitation in each rainfall event).

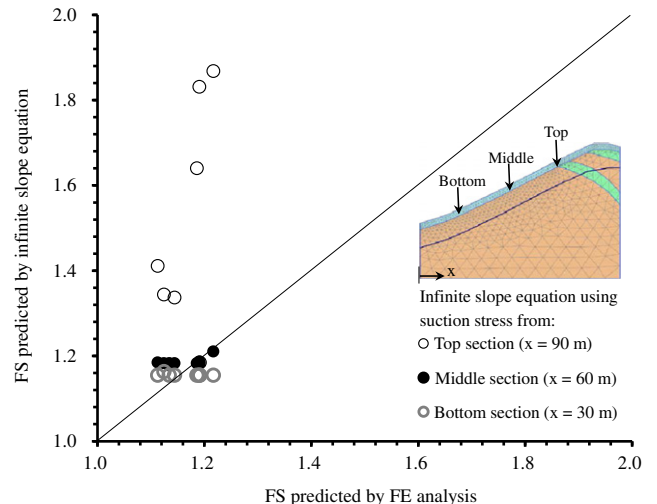


Fig. 17. Comparison between FS predicted by infinite slope equation and FE analysis.

Fig. 17 displays comparison results of the FS predicted by FE analysis (Fig. 12) and the infinite slope equation for eight rainfall events. The comparison results indicate that the infinite slope equation involving the suction stress at the top section of the slope produced higher slope FSs than those involving FE analysis. The FSs predicted using the infinite slope equation correspond with the FSs involving FE analysis when the suction stress at the middle section of the slope was considered. The infinite slope equation may underestimate the FSs at $FS > 1.2$ compared to those involving FE analysis when the suction stress at the bottom section of slope was used as input PWP. Overall, the use of suction stress at the middle and bottom sections of the slope produced more accurate predictions than did the use of suction stress at the top section of the slope. This is because the accumulated PWP increased from the top to the bottom of the slope because of the developed lateral seepage along the soil–rock interface; as a result, high PWP at the lower half of the slope could dominate the stability conditions of the slope and consequently govern the critical FS of the slope.

As discussed above, although soil suction and PWP directly affected slope stability, determining a representative PWP as an input value for the infinite slope equation is crucial because the FS predicted by the infinite slope equation could be critically dependent on the input PWP value. The comparison results in Fig. 17 demonstrated that the infinite slope equation involving the PWP obtained from the lower half of the slopes is applicable for evaluating slope stability.

7. Conclusions

This paper presents a case study and numerical analyses that investigate the failure and deformation mechanism of two unstable slopes subject to rainfall infiltration. Coupled hydro-mechanical FE analyses were conducted based on unsaturated soil mechanics and the generalized effective stress principle, which allows to account for changes in soil moisture and effective stress caused by transient, unsaturated flow. The hydrological response and stress information obtained from the validated numerical models was examined and discussed. The following conclusions were drawn from the results presented in this study:

1. This study demonstrated that by using recorded rainfall, measured soil parameters, site geology, and slope geometry, hydro-mechanical analysis is capable of accurately predicting the failure, timing, and deformation of unsaturated slopes under transient seepage conditions. Moreover, hydro-mechanical analysis can be effectively used to identify the underlying mechanism of the effects of rainfall infiltration on slope instability.
2. The failure of Slope 1 (failure case) was attributed to the rainfall-induced wetting front advancement. When the wetting front passed, the soil became fully saturated. The PWP of surficial soil changed from negative to positive, causing suction losses, further leading to a decrease in soil shear strength. The stress path of soil moved to the lower left in the p' - q space, indicating that the soil effective stress decreased as infiltration progressed, and eventually the soil stress path contacted the K_f line at the limit state, indicating the failure of the slope.
3. The numerical results of Slope 2 (excessive deformation case) suggested that the slope FS varied with wetting and drying cycles. The development of permanent deformation was caused by the accumulation of positive PWP at the soil–rock interface. Nonuniform lateral flows parallel to the interface were observed, leading to an increase of PWP from the upper to the lower slope. The soil stress path moved parallel to the p' axis under drying and wetting cycles.
4. Considering the effect of suction in the generalized effective stress principle enables a clear presentation of the stress path and a unified failure envelope in the two-dimensional p' - q space.
5. Examination of the relationships between the slope FS and the corresponding hydrological data (i.e., rainfall and soil PWP) indicated that

the FS is positively correlated with the accumulated rainfall, rather than the maximum 24-h rainfall in one rainfall event.

6. Determining a representative PWP as an input value for the infinite slope equation is crucial because the FS predicted by the infinite slope equation could significantly vary with the input of the PWP value. This study demonstrated that the infinite slope equation involving the PWP obtained from the lower half of the slope could generate accurate FS prediction results.

For the purpose of effective risk management, coupled hydro-mechanical analysis combined with detailed site investigation could be performed to establish the FS vs. accumulated rainfall relationship for slopes which could affect major protected properties or residents. The results of the analyses provide a valuable reference for identifying and assessing potential hazardous sources to subsequently formulate disaster prevention and mitigation strategies (e.g., establishing early warning systems and evacuation plans or applying engineering approaches to enhance slope stability to reduce rainfall infiltration).

Notation

Basic SI units are given in parenthesis.

\underline{C}	coupling matrix (dimensionless)
c'	effective cohesion of saturated soil (Pa)
E	soil modulus (Pa)
E_{50}	soil moduli at 50% of stress level (Pa)
E_{50}^{ref}	reference modulus (Pa)
E_i	initial soil modulus (Pa)
E_{oed}^{ref}	tangent oedometer loading modulus (Pa)
E_{sat}	saturated soil modulus (Pa)
E_{ur}^{ref}	unloading-reloading modulus (Pa)
f_u	vector corresponding to external load increment (N)
g	acceleration due to gravity (m/s^2)
\underline{G}	vector corresponding to the vertical flow driven by gravity (m^3/s)
H	depth of the sliding plane (m)
\underline{H}	permeability matrix (m/s)
h	total hydraulic head (m)
h_p	pressure head (m)
I	rainfall intensity (m/s)
\underline{K}	stiffness matrix (N/m)
k	hydraulic conductivity (m/s)
k_{rel}	relative hydraulic conductivity (dimensionless)
k_s	saturated hydraulic conductivity (m/s)
$k_{s,h}$	soil saturated horizontal hydraulic conductivity (m/s)
$k_{s,v}$	soil saturated vertical hydraulic conductivity (m/s)
k_x	hydraulic conductivity in x-direction (m/s)
k_y	hydraulic conductivity in y-direction (m/s)
m	modulus exponent
m_w	coefficient of water volume change (dimensionless)
n	fitting parameter for van Genuchten equations (dimensionless)
p	net total stress (Pa)
\underline{p}	vector corresponding to pore pressure (Pa)
p'	net effective stress (Pa)
p_a	atmospheric pressure (Pa)
\underline{Q}	coupling matrix (dimensionless)
\underline{q}	deviatoric stress (Pa)
\underline{q}_p	vector corresponding to input flux on boundaries (m/s)
q_u	uniaxial compression strength (Pa)
R_f	failure ratio (dimensionless)
S	degree of saturation (dimensionless)
\underline{S}	compressibility matrix (Pa^{-1})
\underline{S}_e	effective saturation (dimensionless)
S_r	degree of saturation at residual state (dimensionless)

S_s	degree of saturation at fully saturated state (dimensionless)
t	time (s)
\underline{u}	vector corresponding to incremental deformation (m)
u_a	pore air pressure (Pa)
u_w	pore water pressure (Pa)
α	fitting parameter for van Genuchten equations (Pa^{-1})
α_f	coefficient to account for fine content (dimensionless)
β	slope angle ($^\circ$)
ϕ'	effective friction angle ($^\circ$)
γ	unit weight of soil (N/m^3)
γ_{unsat}	unit weight of unsaturated soil (N/m^3)
γ_{sat}	unit weight of saturated soil (N/m^3)
Θ	normalized volumetric water content (dimensionless)
θ	volumetric water content (dimensionless)
θ_r	residual volumetric water content (dimensionless)
θ_s	saturated volumetric water content (dimensionless)
ρ_w	density of water (kg/m^3)
σ	total stress (Pa)
σ'	effective stress (Pa)
σ^s	suction stress (Pa)
τ	soil shear strength (Pa)
ψ	soil dilation angle ($^\circ$)
ν'	Poisson's ratio

Abbreviations

CL	low plastic clay
F	residual layer
FE	finite element
FS	factor of safety
GP	Guelph permeameter
GWT	ground water table
K_f	unified failure envelope
MIT	Massachusetts Institute of Technology
ML	low plastic silt
PI	plasticity index
PWP	pore water pressure
SH	shale
SH/ss	shale interbedded with few sandstone
SP	silty sand
SPT	standard penetration test
SS	sandstone
SSCC	suction stress characteristic curve
SS-SH	sandstone-shale interbedded layer
SWCC	soil water characteristic curve
USDA	United States Department of Agriculture

Acknowledgements

This research work was sponsored by the National Taiwan University of Science and Technology-Tokushima University Joint Research Program. The financial support for the third author during his Ph.D. study was provided by the Taiwan Ministry of Education under the grant for "Aim for the Top-Tier University Project". These financial supports are gratefully acknowledged. The authors also sincerely appreciate the Taiwan Professional Geotechnical Engineers Association for providing the detailed information for the case study in this paper.

References

- Alonso, E.E., Gens, A., Josa, A., 1990. A constitutive model for partially saturated soils. *Geotechnique* 40, 405–430.
- Alonso, E.E., Gens, A., Lloret, A., Delahaye, C., 1995. Effect of rain infiltration on the stability of slopes. *Proceedings of the First International Conference on Unsaturated Soils, UNSAT'95*, Paris, France, pp. 241–249.
- Alonso, E.E., Gens, A., Delahaye, C.H., 2003. Influence of rainfall on the deformation and stability of a slope in overconsolidated clays: a case study. *Hydrogeol. J.* 11 (1), 174–192.
- Baeza, C., Corominas, J., 2001. Assessment of shallow landslide susceptibility by means of multivariate statistical techniques. *Earth Surf. Process. Landf.* 26 (12), 1251–1263.
- Biot, M.A., 1941. General theory of three dimensional consolidation. *J. Appl. Phys.* 12, 155–164.
- Bishop, A.W., 1954. The use of pore-pressure coefficients in practice. *Geotechnique* 4 (4), 148–152.
- Blake, J.R., Renaud, J.P., Anderson, M.G., Hencher, S.R., 2003. Prediction of rainfall-induced transient water pressure head behind a retaining wall using a high-resolution finite element model. *Comput. Geotech.* 30 (6), 431–442.
- Bolton, M.D., 1986. The strength and dilatancy of sands. *Geotechnique* 36 (1), 65–78.
- Borja, R.I., White, J.A., Liu, X., Wu, W., 2012. Factor of safety in a partially saturated slope inferred from hydro-mechanical continuum modeling. *Int. J. Numer. Anal. Methods Geomech.* 36 (2), 236–248.
- Cai, F., Ugai, K., 2004. Numerical analysis of rainfall effects on slope stability. *Int. J. Geomech.* 4 (2), 69–78.
- Casini, F., 2013. Coupled processes during rainfall- an experimental investigation on a silty sand. *Poromechanics*. ASCE, pp. 1542–1549.
- Chen, J.F., Yeh, H.F., Lee, C.H., Lo, W.C., 2005. Optimal Comparison of Empirical Equations for Estimating Potential Evapotranspiration in Taiwan. XXXI IAHR CONGRESS, Seoul, Korea, pp. 3687–3697.
- Chen, R.H., Chen, H.P., Chen, K.S., Zhong, H.B., 2009. Simulation of a slope failure induced by rainfall infiltration. *Environ. Geol.* 58 (5), 943–952.
- Chen, H.X., Zhang, L.M., Gao, L., Zhu, H., Zhang, S., 2015. Presenting regional shallow landslide movement on three-dimensional digital terrain. *Eng. Geol.* 195, 122–134.
- Cho, S.E., 2014. Probabilistic stability analysis of rainfall-induced landslides considering spatial variability of permeability. *Eng. Geol.* 171, 11–20.
- Cho, S.E., 2016. Stability analysis of unsaturated soil slopes considering water-air flow caused by rainfall infiltration. *Eng. Geol.* 211, 184–197.
- Cho, S.E., Lee, S.R., 2001. Instability of unsaturated soil slopes due to infiltration. *Comput. Geotech.* 28 (3), 185–208.
- Cho, S.E., Lee, S.R., 2002. Evaluation of surficial stability for homogeneous slopes considering rainfall characteristics. *J. Geotech. Geoenviron.* 128 (9), 756–763.
- Collins, B.D., Znidarcic, D., 2004. Stability analyses of rainfall induced landslides. *J. Geotech. Geoenviron.* 130 (4), 362–372.
- Da Costa, A., Sagasetta, C., 2010. Analysis of shallow instabilities in soil slopes reinforced with nailed steel wire meshes. *Eng. Geol.* 113, 53–61.
- Davies, O., Rouainia, M., Glendinning, S., Cash, M., Trento, V., 2014. Investigation of a pore pressure driven slope failure using a coupled hydro-mechanical model. *Eng. Geol.* 178, 70–81.
- Ehlers, W., Graf, T., Ammann, M., 2004. Deformation and localization analysis of partially saturated soil. *Comput. Methods Appl. Mech. Eng.* 193 (27–29), 2885–2910.
- Eichenberger, J., Nuth, M., Laloui, L., 2011. Modeling the onset of shallow landslides in partially saturated slopes. *Geo-Frontiers 2011*. ASCE, pp. 1672–1682.
- Galavi, V., 2010. Groundwater Flow Fully Coupled Flow Deformation and Undrained Analyses in PLAXIS 2D and 3D. PLAXIS internal research report. p. 290.
- Gerscovich, D.M.S., Vargas, E.A., de Campos, T.M.P., 2006. On the evaluation of unsaturated flow in a natural slope in Rio de Janeiro, Brazil. *Eng. Geol.* 88 (1–2), 23–40.
- Godt, J.W., Baum, R.L., Lu, N., 2009. Land sliding in partially saturated materials. *Geophys. Res. Lett.* 36, 1–5.
- Goodman, R.E., 1989. *Introduction to Rock Mechanics*. second ed. Wiley.
- Gui, M.W., Wu, Y.M., 2014. Failure of soil under water infiltration condition. *Eng. Geol.* 181, 124–141.
- Hayashi, M., Quinton, W.L., 2004. A constant-head well permeameter method for measuring field-saturated hydraulic conductivity above an impermeable layer. *Can. J. Soil Sci.* 84 (3), 255–264.
- Hossain, J., Hossain, M.S., Hoyos, L.R., 2013. Effect of rainfall on stability of unsaturated earth slopes constructed on expansive clay. *ASCE Geo-congress*, pp. 417–425.
- Hsu, K.-C., Wang, C.-H., Chen, K.-C., Chen, C.-T., Ma, K.-W., 2006. Climate-induced hydrological impacts on the groundwater system of the Pingtung Plain, Taiwan. *Hydrogeol. J.* 15 (5), 903–913.
- Huang, C.-C., Lo, C.-L., 2013. Simulation of subsurface flows associated with rainfall-induced shallow slope failures. *J. GeoEng.* 8 (3), 101–111.
- Iryo, T., Rowe, R.K., 2005. Infiltration into an embankment reinforced by nonwoven geotextiles. *Can. Geotech. J.* 42 (4), 1145–1159.
- Kao, Y.H., Liu, C.W., Wang, S.W., Lee, C.H., 2012. Estimating mountain block recharge to downstream alluvial aquifers from standard methods. *J. Hydrol.* 426–427, 93–102.
- Kim, W.S., Borden, R.H., 2013. Numerical simulation of MSE wall behavior induced by surface-water infiltration. *J. Geotech. Geoenviron. Eng. ASCE* 139 (12), 2110–2124.
- Kim, J., Jeong, S., Park, S., Sharma, J., 2004. Influence of rainfall-induced wetting on the stability of slopes in weathered soils. *Eng. Geol.* 75 (3–4), 251–262.
- Kim, B.D., Park, S.W., Takeshita, Y., Kato, S., 2016. Effect of suction stress on critical state of compacted silty soils under low confining pressure. *Int. J. Geomech. ASCE*, D4016010 [http://dx.doi.org/10.1061/\(ASCE\)GM.1943-5622.0000665](http://dx.doi.org/10.1061/(ASCE)GM.1943-5622.0000665).
- Kulhawy, F.H., Mayne, P.W., 1990. *Manual on Estimating Soil Properties for Foundation Design*. Electric Power Research Institute, Palo Alto, California.
- Brinkgreve, R.B.J., Kumaraswamy, S., Swolfs, W.M., 2015. *PLAXIS 2015 Manual*. Balkema, Rotterdam, The Netherlands.
- Lee, J.H., Park, H.J., 2015. Assessment of shallow landslide susceptibility using the transient infiltration flow model and GIS-based probabilistic approach. *Landslides* <http://dx.doi.org/10.1007/s10346-015-0646-6>.
- Lu, N., Likos, W.J., 2004. *Unsaturated Soil Mechanics*. Wiley.
- Lu, N., Likos, W.J., 2006. Suction stress characteristic curve for unsaturated soil. *J. Geotech. Geoenviron.* 132 (2), 131–142.
- Lu, N., Godt, J.W., Wu, D.T., 2010. A closed-form equation for effective stress in unsaturated soil. *Water Resour. Res.* 46, W05515.

- Lu, N., Wayllace, A., Oh, S., 2013. Infiltration-induced seasonally reactivated instability of a highway embankment near the Eisenhower Tunnel, Colorado, USA. *Eng. Geol.* 162, 22–32.
- Matsumaru, T., Uzuoka, R., 2016. Three-phase seepage-deformation coupled analysis about unsaturated embankment damaged by earthquake. *Int. J. Geomech.*, C4016006 [http://dx.doi.org/10.1061/\(ASCE\)GM.1943-5622.0000699](http://dx.doi.org/10.1061/(ASCE)GM.1943-5622.0000699).
- Mori, T., Uzuoka, R., Chiba, T., Kamiya, K., Kazama, M., 2011. Numerical prediction of seepage and seismic behavior of unsaturated fill slope. *Soils Found.* 51 (6), 1075–1090.
- Morse, M.S., Lu, N., Wayllace, A., Godt, J.W., Take, W.A., 2014. Experimental test of theory for the stability of partially saturated vertical cut slopes. *J. Geotech. Geoenviron. Eng.* [http://dx.doi.org/10.1061/\(ASCE\)GT.1943-5606.0001119](http://dx.doi.org/10.1061/(ASCE)GT.1943-5606.0001119).
- Mualem, Y., 1976. A new model for predicting the hydraulic conductivity of unsaturated porous media. *Water Resour. Res.* 12, 593–622.
- Munthar, A.S., Liao, H.J., 2010. Rainfall infiltration: Infinite slope model for landslides triggering by rainstorm. *Nat. Hazards* 54, 967–984.
- Nogueira, C.D.L., Azevedo, R.F., Zornberg, J.G., 2011. Validation of coupled simulation of excavations in saturated clay: camboinhas case history. *Int. J. Geomech.* 11 (3), 202–210.
- Oh, S., Lu, N., 2015. Slope stability analysis under unsaturated conditions: case studies of rainfall-induced failure of cut slopes. *Eng. Geol.* 184, 96–103.
- Qi, S., Vanapalli, S.K., 2015. Hydro-mechanical coupling effect on surficial layer stability of unsaturated expansive soil slopes. *Comput. Geotech.* 70, 68–82.
- Rahardjo, H., Lim, T.T., Chang, M.F., Fredlund, D.G., 1995. Shear strength characteristics of a residual soil. *Can. Geotech. J.* 32, 60–77.
- Reynolds, W.D., Elrick, D.E., Baumgartner, N., Clothier, B.E., 1984. The Guelph Permeameter for measuring the field-saturated hydraulic conductivity above the water table: 2. The apparatus. *Proceedings of Canadian Hydrology Symposium*.
- Reynolds, W.D., Elrick, D.E., Clouthier, B.E., 1985. The constant head well permeameter: effect of unsaturated flow. *Soil Sci.* 139, 172–180.
- Richards, L.A., 1931. Capillary conduction of liquids through porous mediums. *Physics* 1, 318–333.
- Rojas, E., Pérez-Rea, M., López-Lara, T., Hernández, J., Horta, J., 2015. Use of effective stresses to model the collapse upon wetting in unsaturated soils. *J. Geotech. Geoenviron. Eng.*, 04015007 [http://dx.doi.org/10.1061/\(ASCE\)GT.1943-5606.0001251](http://dx.doi.org/10.1061/(ASCE)GT.1943-5606.0001251).
- Schanz, T., Vermeer, P.A., Bonnier, P.G., 1999. The hardening soil model-formulation and verification. *Beyond 2000 in Computational Geotechnics- 10 Years of PLAXIS*, Balkema, Rotterdam.
- Schmertmann, J.H., 1970. Static cone to compute static settlement over sand. *J. Soil Mech. Found. Div. ASCE* 96 (SM3), 1011–1043.
- Sheng, D., Gens, A., Fredlund, D.G., Sloan, S.W., 2008. Unsaturated soils: from constitutive modelling to numerical algorithms. *Comput. Geotech.* 35, 810–824.
- Thuo, J.N., Yang, K.H., Huang, C.C., 2015. Infiltration into unsaturated reinforced slopes with nonwoven geotextile drains sandwiched in sand layers. *Geosynth. Int.* 22 (6), 457–474.
- Urciuoli, G., Pirone, M., Comegna, L., Picarelli, L., 2016. Long-term investigations on the pore pressure regime in saturated and unsaturated sloping soils. *Eng. Geol.* 212, 98–119.
- van Genuchten, M.T., 1980. A closed form equation for predicting the hydraulic conductivity of unsaturated soils. *Soil Sci. Soc. Am. J.* 44 (5), 892–898.
- Vanapalli, S.K., Fredlund, D.G., Pufahl, D.E., Clifton, A.W., 1996. Model for the prediction of shear strength with respect to soil suction. *Can. Geotech. J.* 33 (3), 379–392.
- VandenBerge, D.R., J.M., D., Brandon, T.L., 2015. Limitations of transient seepage analyses for calculating pore pressures during external water level changes. *J. Geotech. Geoenviron. Eng. ASCE* 141 (1), 1–10.
- Wu, Y.M., Lan, H.X., Gao, X., Li, L.P., Yang, Z.H., 2015a. A simplified physically based coupled rainfall threshold model for triggering landslides. *Eng. Geol.* 195, 63–69.
- Wu, L.Z., Zhang, L.M., Li, X., 2015b. One-dimensional coupled infiltration and deformation in unsaturated soils subjected to varying rainfall. *Int. J. Geomech. ASCE* [http://dx.doi.org/10.1061/\(ASCE\)GM.1943-5622.0000535](http://dx.doi.org/10.1061/(ASCE)GM.1943-5622.0000535).
- Yang, K.-H., Yalaw, W.M., Nguyen, M.D., 2016a. Behavior of geotextile-reinforced clay with a coarse material sandwich technique under unconsolidated-undrained triaxial compression. *Int. J. Geomech.* 16 (3). [http://dx.doi.org/10.1061/\(ASCE\)GM.1943-5622.0000611](http://dx.doi.org/10.1061/(ASCE)GM.1943-5622.0000611).
- Yang, K.-H., Nguyen, M.D., Yalaw, W.M., Liu, C.-N., Gupta, R., 2016b. Behavior of geotextile-reinforced clay under consolidated-undrained tests: reinterpretation of porewater pressure parameters. *J. Geoenviron. Eng.* 11 (2), 45–57.
- Yoo, C., Jung, H.-Y., 2006. Case history of geosynthetic reinforced segmental retaining wall failure. *J. Geotech. Geoenviron. Eng. ASCE* 132 (12), 1538–1548.
- Zhang, L.L., Zhang, L.M., Tang, W.H., 2005. Rainfall-induced slope failure considering variability of soil properties. *Geotechnique* 55 (2), 183–188.
- Zhang, L.L., Fredlund, D.G., Fredlund, M.D., Wilson, G.W., 2014. Modeling the unsaturated soil zone in slope stability. *Can. Geotech. J.* 51 (12), 1384–1398.